

МЕДНО-МОЛИБДЕН-ПОРФИРОВОЕ МЕСТОРОЖДЕНИЕ КИГАЛ (Северо-Западный Иран): ПРЕДСТАВЛЕНИЕ О ПРОИСХОЖДЕНИИ И ЭВОЛЮЦИИ МИНЕРАЛИЗУЮЩИХ ФЛЮИДОВ

С. Хасанпур¹, С. Раджабпур²

¹ Department of Geology, Payame Noor University, Nakhi st., Lashkarak Highway, Tehran, 19569, Iran

² Instituto de Geología Económica Aplicada (GEA), Universidad de Concepción, Casilla 160-C, Concepción, Chile

Медно-молибден-порфировое месторождение Кигал с координатами 46°42'36" с.ш. и 38°37'06" в.д. расположено в 120 км к северу от г. Тебриз и в 12 км к северу от г. Варзеган в магматическом поясе Арасбаран в Северо-Западном Иране. Геологическими единицами в Кигальском районе являются эоценовые и олигоценные вулканические породы в ассоциации с миоценовыми интрузивными и субвулканическими породами. Кварц-монзонитовые порфиры в Кигальском районе вмещают медно-молибден-порфировую минерализацию, включающую четыре зоны изменения: калиевую, гидротермальную, аргиллитовую и пропилитовую, а также многочисленные кварцевые прожилки. По минералогическим и геохимическим данным интрузивные и субвулканические породы относятся к кварц-диоритовым, диоритовым и гранитным образованиям с составом, варьирующим от высококалиевого кальциево-щелочного до кальциево-щелочного. Все образцы обогащены крупноионными литофильными элементами и обеднены высокозарядными элементами, что указывает на загрязнение мантийно-магматического источника материалом субдуцированной океанической коры. Три типа флюидных включений выявлены в кварце из разных кварц-сульфидных прожилков: многофазные (LVS) и преимущественно жидкие (LV) включения в калиевой зоне, преимущественно жидкие (LV) и преимущественно паровые (VL) включения в гидротермальной зоне и преимущественно жидкие (LV) включения в кремнезёмистой зоне. Микротермометрические исследования показали, что температура гомогенизации ($T_{\text{гом}}$) многофазных флюидных включений в калиевой зоне изменяется от 265 до 450 °С, а солёность — от 38 до 59 мас.% NaCl-экв. Эти значения выше, чем соответствующие значения для двухфазных флюидных включений в гидротермальной зоне ($T_{\text{гом}}$ от 163 до 466 °С, солёность от 0.3 до 11 мас.% NaCl-экв.). Рассчитанные значения $\delta^{18}\text{O}_{\text{H}_2\text{O}}$ и $\delta\text{D}_{\text{H}_2\text{O}}$ для биотита, серицита и кварца из калиевой, гидротермальной и кремнезёмистой зон показали, что минерализация в калиевой зоне обусловлена главным образом магматической водой и в меньшей степени метеорной. Пониженные значения $\delta\text{D}_{\text{H}_2\text{O}}$ для биотита калиевой зоны могут быть связаны с дегазацией магмы и/или изменением состава флюида с притоком магматической воды в гидротермальную систему.

Флюидные включения, изотопы кислорода и водорода, медно-молибден-порфировое месторождение Кигал, магматический пояс Арасбаран, Северо-Западный Иран.

THE KIGHAL PORPHYRY Cu–Mo DEPOSIT, NW IRAN: INSIGHTS INTO ORIGIN AND EVOLUTION OF THE MINERALIZING FLUIDS

S. Hassanpour, S. Rajabpour

The Kighal porphyry Cu–Mo deposit, located at 46°42'36" N and 38°37'06" E, occurs 120 km north of Tabriz and 12 km north of Varzeghan in the Arasbaran magmatic belt, NW Iran. The geologic units in the Kighal area are Eocene and Oligocene volcanic rocks associated with Miocene intrusive and subvolcanic rocks. Quartz-monzonite porphyry in the Kighal area hosts porphyry style Cu–Mo mineralization consisting of four alteration zones (potassic, phyllic, argillic, and propylitic) and abundant quartz veinlets. Based on mineralogy and geochemistry data, the intrusive and subvolcanic rocks belong to quartz-diorite, diorite, and granite units with high-K calc-alkaline to calc-alkaline affinities. All samples are enriched in LILE and depleted in HFSE, pointing to a mantle magma source contamination with subducted oceanic-crust material. Three types of fluid inclusions are identified in quartz from different quartz–sulfide veinlets, including multiphase (LVS) and liquid-rich (LV) inclusions in the potassic zone, liquid-rich (LV) and vapor-rich (VL) inclusions in the phyllic zone, and liquid-rich (LV) inclusions in the silicic zone. Microthermometry studies showed that T_h in multiphase fluid inclusions in the potassic zone varied from 265 to 450 °C and salinity, from 38 to 59 wt.% NaCl-equiv. These values are higher than those of two-phase fluid inclusions in the phyllic zone (T_h of 163 to 466 °C and salinity of 0.3 to 11 wt.% NaCl-equiv.). The calculated $\delta^{18}\text{O}_{\text{H}_2\text{O}}$ and $\delta\text{D}_{\text{H}_2\text{O}}$ values in biotite, sericite, and quartz from potassic, phyllic, and silicic zones showed that it is predominantly magmatic water with a lesser amount of meteoric water that is responsible for mineralization in the potassic zone. Light $\delta\text{D}_{\text{H}_2\text{O}}$ values of biotite in the potassic zone suggest a magma degassing process and/or a change in the fluid composition with magmatic water influx to a hydrothermal system.

Fluid inclusions, O–H isotopes, Kighal porphyry Cu–Mo deposit, Arasbaran magmatic belt, NW Iran

INTRODUCTION

The majority of the known porphyry-type Cu \pm Mo deposits in Iran occurred in a Cenozoic volcanoplutonic belt known as Urmieh–Dokhtar Magmatic Belt. The belt extends for over 2000 km, with an average width of 50 km, from the northwest to the southeast of Iran. The development of the belt is considered to be associated with the subduction of the Neotethys oceanic lithosphere underneath central Iran, and the collision of the African and Eurasian plates during the Alpine orogeny in the Tertiary (Niazi et al., 1978; Berberian and King, 1981; Pourhosseini, 1981; Stampfli, 2000; Omrani et al., 2008). The northern section of the belt, known as Qaradagh Belt (Berberian and King, 1981; Hassanpour, 2010; Hassanpour et al., 2015), or Arasbaran Metallogenic Zone (AMZ), hosts major porphyry-style Cu–Mo deposits, represented by Sungun, Haftcheshmeh, Kighal and Niaz (Fig. 2), skarn-type base metal deposits, represented by Sungun, Mazraeh, Anjerd (Hassanpour, 2010), and epithermal precious metal deposits, exemplified by Sharafabad, Masjed–Daghi, Sarikhanloo and Safikhanloo (Alirezaei et al., 2008). Compared to the Kerman Belt, however, the evolution of the Qaradagh Belt is poorly known.

The Sungun deposit, with an approved reserve of 500 Mt at 0.69% Cu and ~250 ppm Mo, is the largest known porphyry Cu–Mo system in the AMZ (e.g., (Mehrparto, 1993; Hezarkhani et al., 1997; Calagari, 1997, 2003; NICICO, 2006)). The Haftcheshmeh deposit showed a preliminary appraisal with a reserve of 300 Mt at 0.38% Cu and 0.0350% Mo (Hassanpour et al., 2015). Kighal and Niaz have been approved to be subeconomic reserves (NICICO, 2006). The Kighal porphyry copper deposit was discovered in 2006 by the National Iranian Copper Industries Company (NICICO) who carried out systematic geology, geochemistry and geophysical studies and drilled several exploratory boreholes in the Kighal area. Preliminary studies of geology and fluid inclusions with a few samples for sulfur isotopes in the Kighal deposit were conducted by Simmonds et al. (2012, 2015). Hassanpour (2010) and Hassanpour et al. (2015) also reported Ar–Ar dating for the Kighal intrusive porphyry and compared the results with other deposits in the Arasbaran region.

In this contribution, we have presented new fluid inclusion (FIs) and O–H isotopes data for the Kighal deposit in an effort to better understand the origin and evolution of the mineralizing hydrothermal fluids. FIs study in porphyry copper systems is an important tool for determination of physicochemical conditions of hydrothermal fluids that are responsible for pervasive alteration and related mineralization processes (Richards, 2011). Determination of $^{18}\text{O}/^{16}\text{O}$ and D/H ratios indicated a fundamental role of magmatic water in the mineralization and alteration systems, especially in the central parts of the porphyry systems.

REGIONAL GEOLOGY

The Urmieh–Dokhtar Magmatic Arc (UDMA) and Arasbaran Magmatic Zone (AMZ) are two major copper belts in Iran situated on the Alpine orogenic belt (Fig. 1). These belts are known as areas with a high potential for porphyry type Cu \pm Mo \pm Au systems in Iran (Shafiei et al., 2009; Hassanpour, 2010). Porphyry copper deposits in the Arasbaran region mainly developed in the last stage of Meso–Tethys Oceanic closure with intrusions and replacement of Oligo–Miocene intrusive bodies (Fig. 2) (Hassanpour, 2010; Sohrabi, 2015). The AMZ in the NW of Iran has been considered as one of the most important Cu–Mo–Au metallogenic province where introduced by the GSI as the “Ahar–Arasbaran zone” and “Qareh–Dagh belt” by Berberian and King (1981) and the Arasbaran Magmatic Belt by Hassanpour (2010) (Fig. 2). This zone is one of the most important parts of porphyry copper and epithermal gold deposits which formed in an arc setting on the southern margin of the Lesser Caucasus. The Sungun porphyry copper deposit as well as other deposits (Haftcheshmeh, Niaz, Sheleboran in Iranian side and Kadjeran and Dastakert in Armenian side) occurred on this magmatic arc (Fig. 2).

The main geologic units in the Arasbaran copper belt are Eocene to upper Pleistocene volcanic and volcanosedimentary rocks with a Cretaceous basement (including limestones, volcanosedimentary and metamorphic rocks) (Fig. 2). The tectonic activities have been started from the Late Cretaceous–Paleocene times with characteristics of calc-alkaline to tholeiitic magma series in a thin continental crust, close to the theoretical Meso–Tethys trenches and continued with shoshonitic magmatism in the Late Eocene–Oligocene. The main mineralization in this belt occurred at the late Oligocene (e.g., Haftcheshmeh deposit) and early Miocene (e.g., Sungun, Kighal, Sheleboran and Niaz deposits) (Hassanpour, 2010).

LOCAL GEOLOGY IN THE KIGHAL AREA

Geologic features in the Kighal area, in terms of geology and rock properties are similar to those units that outcrop in the Sungun area (Figs. 2 and 4). Igneous rock series belong to the upper Eocene to the Quaternary, ranging from extrusive to intrusive rocks, subvolcanic, pyroclastic and dikes (Figs. 3 and 4). These rocks have acidic to moderate affinities and ranging in composition from latite-andesite to rhyolites which are typically affected by weak to intense different types of alterations. Oligocene magmatic activities begun with andesite, tuff, agglomerate, basalt and rhyolite in the area and subsequently magmatic activities changed to granodio-

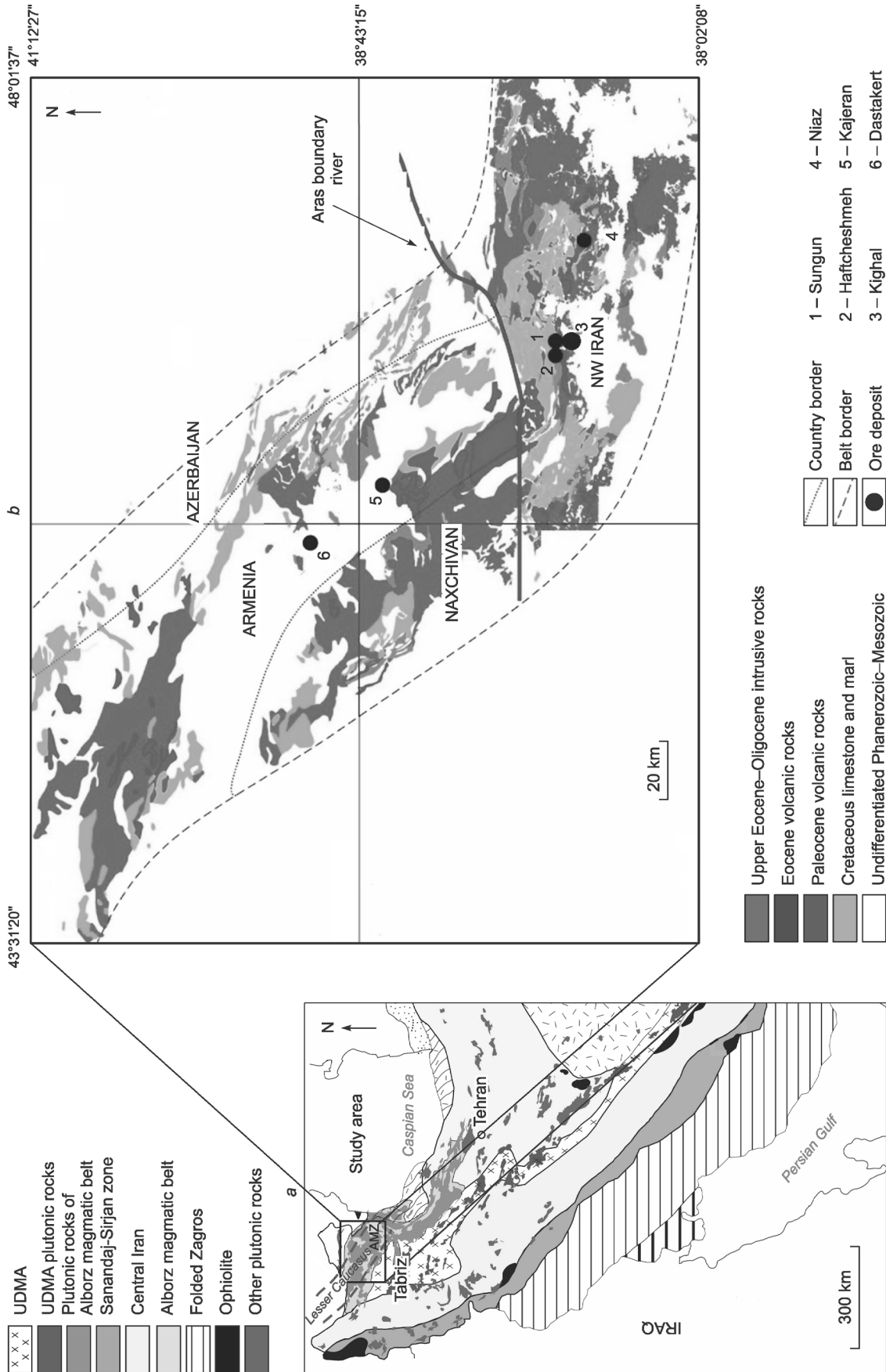


Fig. 1. (a) Schematic geological map of Iran, showing the distribution of the major sedimentary and structural units (after Aghanabati, 1998) and plutonic rocks (after Aghanabati, 1991). The location of the Arasbaran Magmatic Zone (AMZ) and the study area are indicated in the map; (b) simplified geological map of NW Iran and the southern part of Armenia showing major lithologic units with major porphyry systems in the AMZ (modified after (Hassanpour et al., 2015)).

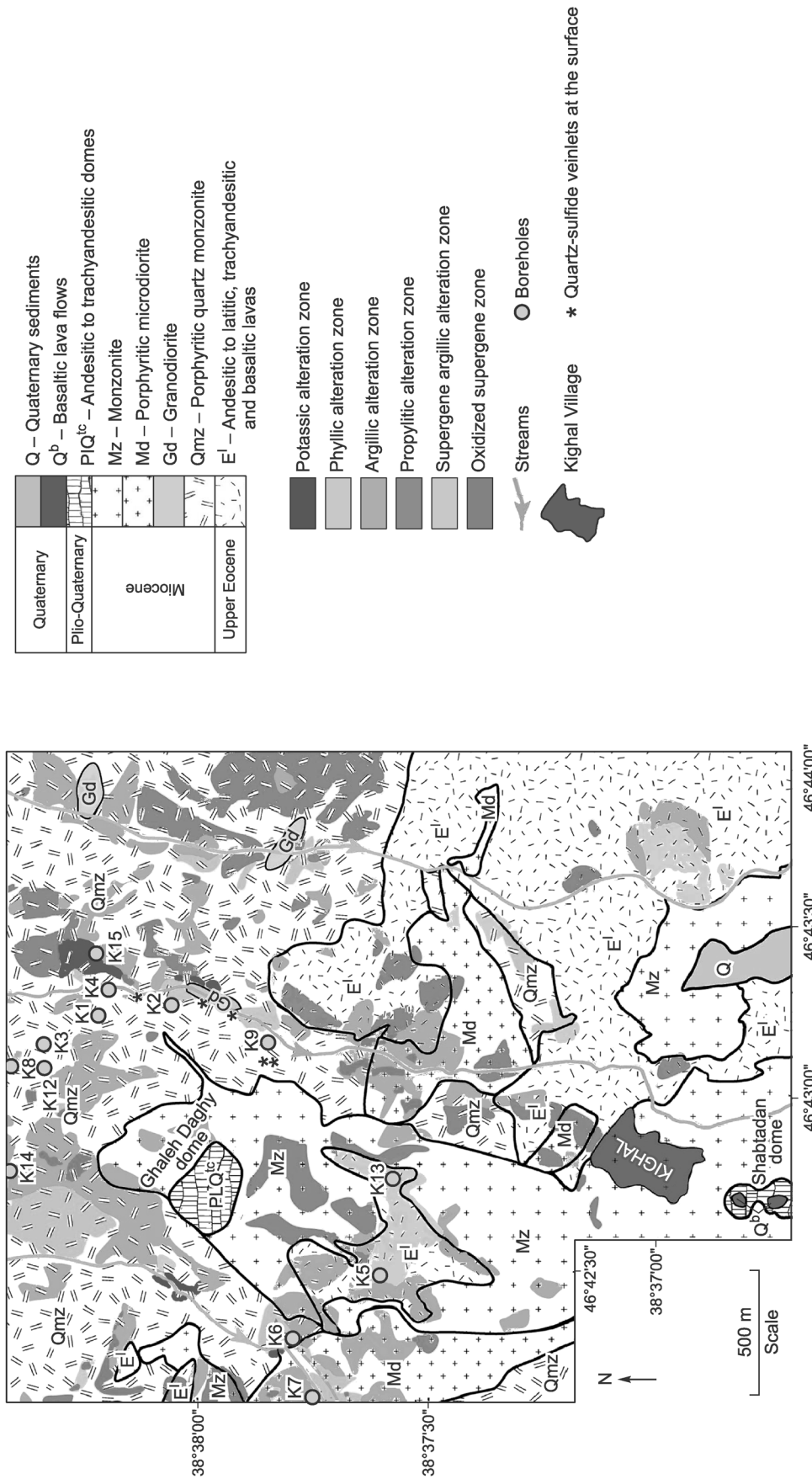


Fig. 2. Geological map of the Kighal deposit (modified after (Simmonds et al., 2015)).

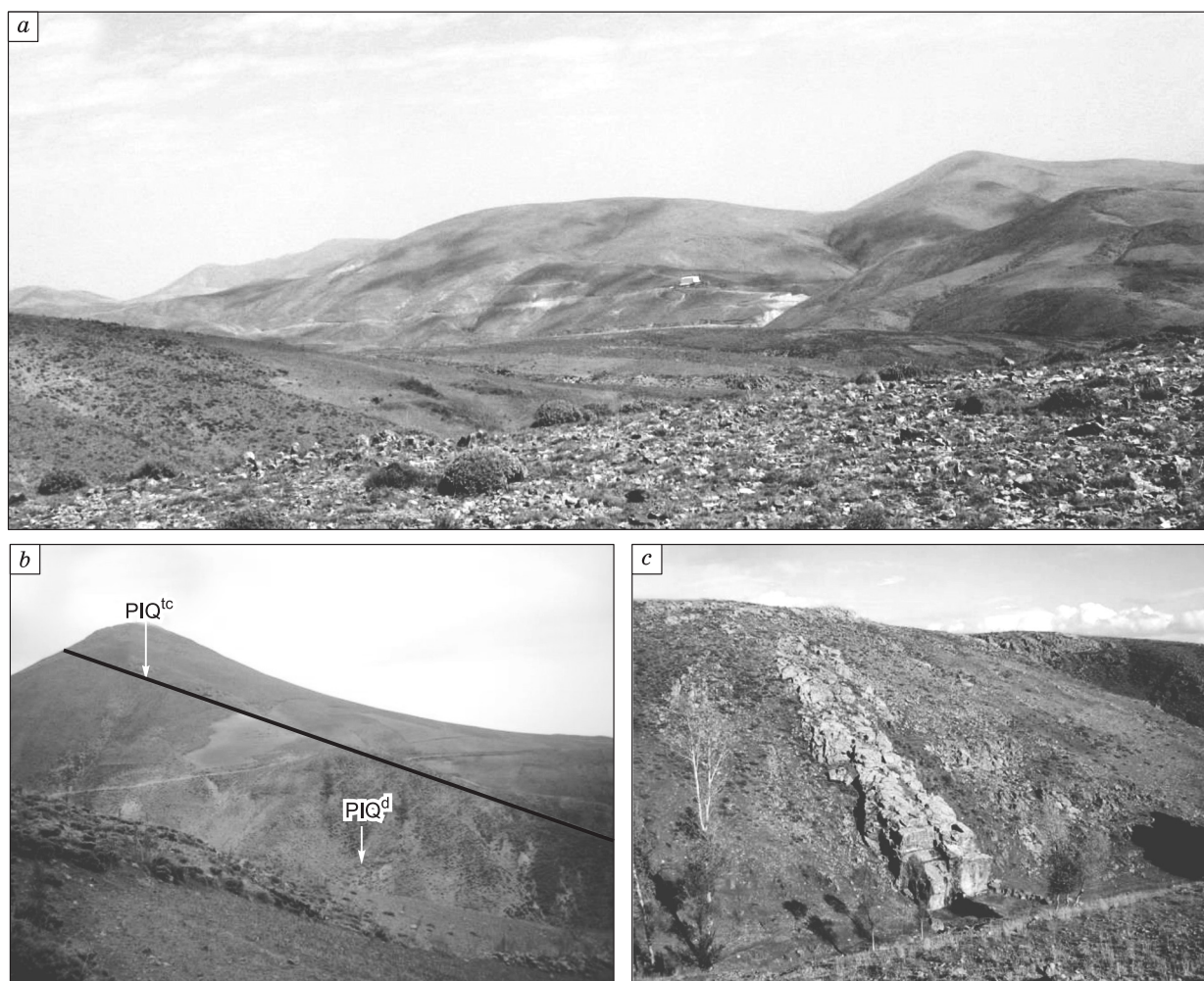


Fig. 3. Field perspective of the Kighal porphyry deposit. (a) an overview of the potassic zone within the Kighal porphyry stock; (b) A view of the country rocks and the Ghaleh-Daghi mountains; (c) the intrusion of dikes with of granodioritic composition within the Kighal stock.

rite and monzodiorite porphyries with subvolcanic natures (Fig. 4a, b). In the Miocene, plutonic activities led to intrusions of quartz-monzonite porphyry stocks mainly in the eastern part of the Kighal and caused extensive hydrothermal alterations in the region. Magmatic activities resumed in the late Miocene, with intrusion of barren granodiorite body and late dikes with diorite to quartz-diorite and monzodiorite. Eventually, the youngest unit of the region occurred as Pliocene–Quaternary basalt to andesite lavas (Fig. 3). The main quartz-monzonite stock, which hosts the porphyry Cu–Mo mineralization, intruded into the upper Eocene andesite-latite and basaltic-andesite volcanic rocks during Pyrenean orogenic activities (late Oligocene to early Miocene) (NICICO, 2006; Hassanpour, 2010; Simmonds, 2013). The porphyry stock is crosscut by three subvolcanic granodiorite to microdioritic/quartz-porphyry bodies, as well as several dikes with quartz-diorite to granodiorite, microdiorite and monzodiorite combinations (Fig. 4a). The geochemical characteristics of the porphyry system with cross-cutting dikes (Fig. 3c) show I type, calc-alkaline to high-K alkaline and peraluminous to metaluminous affinities in a continental margin setting (NICICO, 2006; Simmonds, 2013).

The granodiorite porphyry stock shows quartz-monzodiorite to granodiorite characteristics with porphyritic and granular textures. This rock comprises plagioclase phenocrysts, biotite, wholly chloritized amphibole and coarse- to fine-grained quartz crystals (Fig. 4b) with no mineralization in comparison with quartz-monzonite porphyry stock. Weak sericitic and propylitic alterations are dominant. The granodiorite pluton contacts with the potassic zone of the porphyry system, and shows potassic alteration signatures including the presence of flake-like neobiotite and orthoclase. Sulfide minerals including pyrite with lesser amounts of chalcopyrite and covellite and also Ti-oxides formed as veinlets and filling open spaces. Quartz-pyrite-bearing veinlets (with a thickness of 0.1 to 5 cm) contain pyrite, chalcopyrite and covellite as intergranular and being quickly disappeared away from the contact zones.

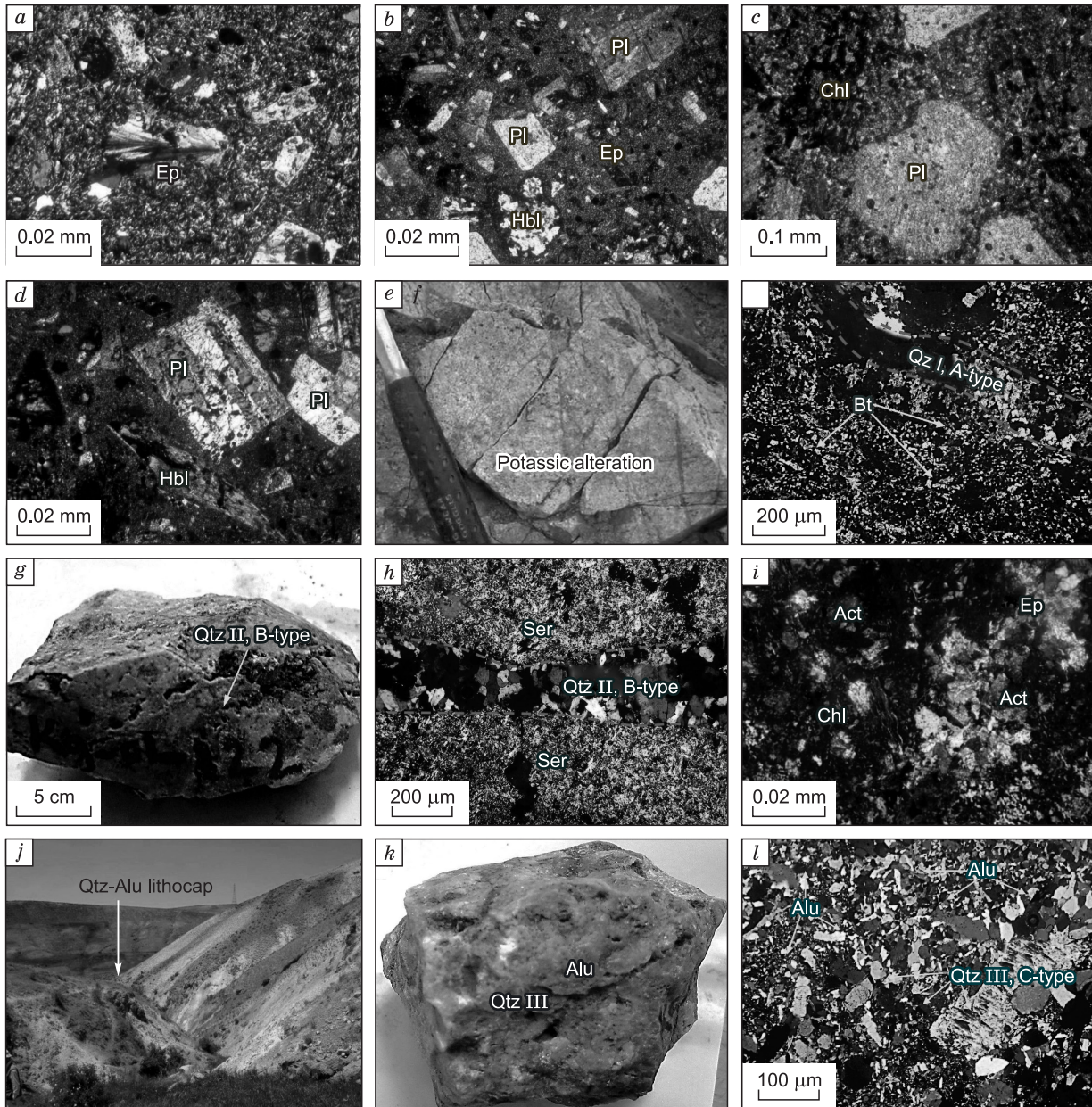


Fig. 4. Photomicrographs of the Kighal porphyry deposit.

(a) The Eocene–Oligocene andesitic rock in the Kighal area with plagioclase phenocrysts and ferromagnesian minerals; (b) granodiorite porphyry; (c) microgranodiorite to micromonzodiorite porphyry; (d) Monzonite unit; (e) Outcrop of the potassic alteration zone in the East of the Kighal area; (f) the potassic zone in the east of the area with secondary biotite and A-type quartz veinlet; (g) D-type quartz veinlet; (h) the phyllic alteration zone which occurs D-type veinlet with sericitic halo; (i) the proplitic alteration zone with abundance epidote and actinolite and chlorite; (j) and (k) silica-alunite lithocap; (l) silica-alunite lithocap. Act, actinolite; Alu, alunite; Bt, biotite; Chl, chlorite; Ep, epidote; Hbl, hornblende; Pl, plagioclase; Qtz, quartz; Ser, sericite.

Microgranodiorite to micromonzodiorite porphyry outcrops in the northeastern part of the Kighal Village and in the center of the study area. The texture of this stock is porphyritic with microgranular matrix and coarse-grained plagioclase, alkali feldspar, amphibole and biotite in addition to quartz, chert fragments and iron oxide/hydroxide spots. Feldspars (plagioclase in most cases) altered to the sericite, muscovite and carbonate in sericitization alteration zone. In addition to argillic alteration, propylitic alteration also occurred in the unit that affected the matrix and feldspar grains and altered them to clay minerals, quartz, chlorite and epidotes (Fig. 4c).

Monzonite porphyry stock is composed of 20 to 30 vol.% of euhedral to subhedral zoned and tabular plagioclase phenocrysts, and 40 to 50 vol.% as microlitic plagioclase in groundmass (Fig. 4d). Plagioclase is accompanied by biotite and amphibole sometimes occupying up to 30 vol.% of the rock as phenocrysts and groundmass. Biotite and amphibole phenocrysts in almost fresh samples are subhedral and slightly replaced by chlorite and opaque minerals. Monzonite porphyry hosts different types of stockwork veinlets and small fractures associated with potassic and phyllic alterations.

HYDROTHERMAL ALTERATION AND MINERALIZATION

Alteration and mineralization were determined by detailed studies of the mineralogy, petrography and geochemical analysis of drill cores and outcrop samples from different parts of the porphyry system and country rocks in the Kighal deposit. Alteration zones have suffered multiple overprinting processes and complexity. Potassic and propylitic alterations are the first developed zones in Kighal followed by phyllic and argillic alterations. Pervasive alteration in the outcrops and drill cores is phyllic alteration which is overprinted on potassic alteration and covers the upper parts of the Kighal porphyry stock. Based on petrography and XRD analysis, phyllic and potassic alterations are mainly recognized in quartz-monzonite porphyry stock. Propylitic alteration is predominantly developed in the country volcanic host rocks (Fig. 4i). The potassic alteration outcrops, indicate a deep erosion of the porphyry system which means most of the upper part of the Kighal deposit has been eroded (Fig. 4e). Quartz-monzonite porphyry stock in terms of mineralization is the most important intrusive body in the Kighal area, belongs to the early Miocene (20 Ma) (Hassanpour, 2010; Hassanpour et al., 2015). Different types of quartz veinlets and four types of alterations including potassic, phyllic, argillic and propylitic occurred in different parts of this stock. The dominant alteration zones of copper mineralization are mainly as potassic and phyllic alterations.

Potassic alteration is restricted to monzonite porphyry, multiple monzonitic dikes, quartz monzonite and granodiorite and as spots outcrops on the surface of the porphyry system. Based on microscopic studies, these

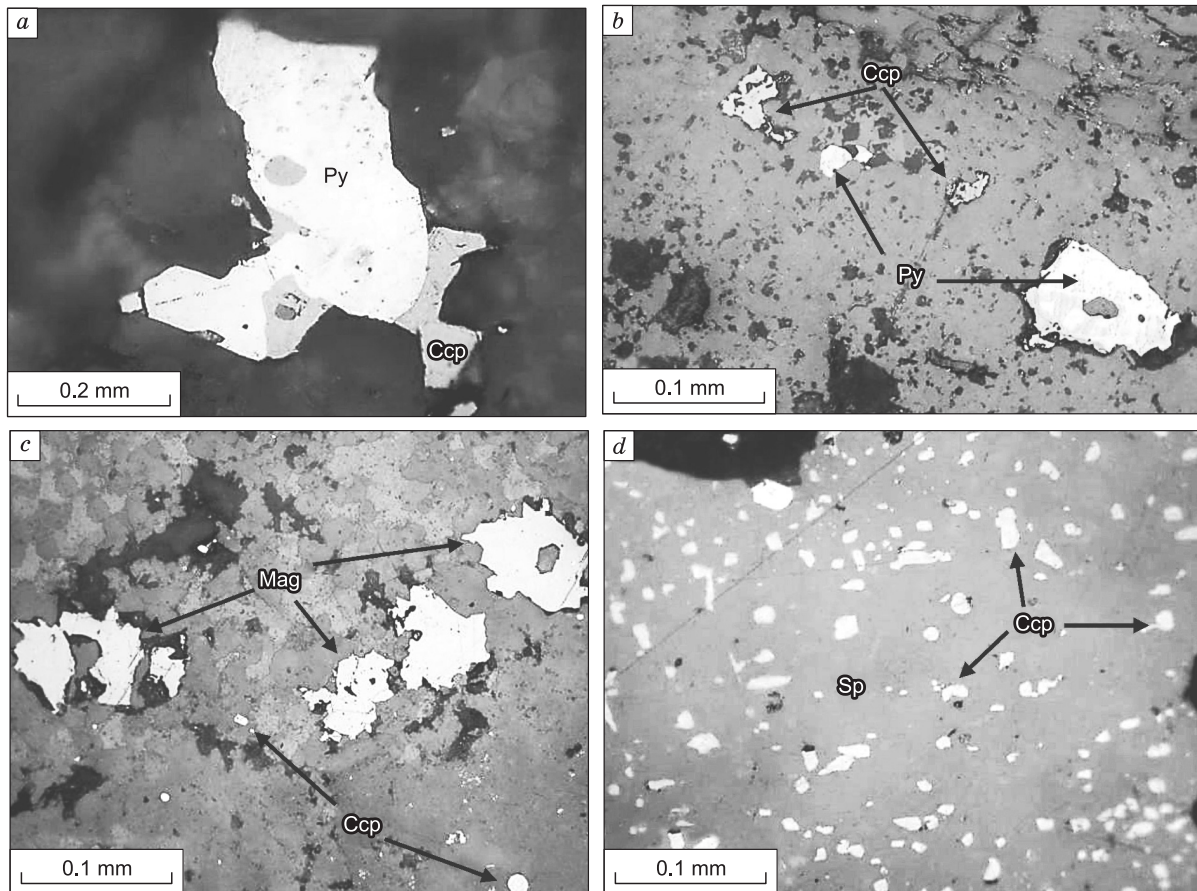


Fig. 5. Photomicrographs of ore minerals from the Kighal deposit.

(a, b) Pyrite crystal replaced by chalcopyrite along borders; (c) disseminated chalcopyrite and magnetite; (d) chalcopyrite crystal coated by sphalerite exsolution. Ccp, chalcopyrite; Sp, sphalerite; Py, pyrite; Mag, magnetite.

rocks vary from quartz-monzodiorite to quartz-monzonite porphyry which has a microgranular matrix and porphyritic texture with coarse-grained plagioclase, K-feldspar, quartz, amphibole and primary fine-grained to secondary coarse-grained euhedral biotite. The potassic alteration in the drill cores mainly composed of secondary hydrothermal biotite (results of replacing primary biotite and amphibole), euhedral fine-grained K-feldspar and sericite (Fig. 4e, f) with opaque minerals including magnetite, pyrite, molybdenite, chalcopyrite and Ti-oxides (Figs. 5a–d).

The phyllic alteration zone contains muscovite and secondary bladed sericite that is an altered product of primary feldspars. Ferromagnesian minerals and plagioclase are partially to completely replaced by sericite and quartz. Veinlets contain pyrite or quartz-pyrite in associated with fine-grained chalcopyrite and covellite formed as disseminated, veinlets and open spaces fillings (Figs. 4g, h), comprising sometimes up to 20 vol.% of the rock. The transitional border between potassic and phyllic alteration zones mixed secondary biotite, K-feldspar, sericite, pyrite and secondary quartz minerals, which indicates that the potassic alteration was progressively replaced by phyllic alteration in the Kighal deposit (Seedorff et al., 2005).

The argillic alteration zone occurred in the fractures and fault zones in the upper parts of the porphyry system. According to the XRD analysis, the main minerals of this alteration include kaolinite, montmorillonite, illite and chlorite. In this alteration zone, feldspar grains altered to clay minerals and sericite. Quartz-sulfide veinlets are rare and only contain small amounts of pyrite in some parts. This zone is overprinted on the phyllic zone.

The propylitic alteration zone outcropped in outermost parts and is more developed in margins and upper parts of the deposit and show a good relationship with argillic and phyllic alteration zones and is recognized by the presence of epidote, chlorite, calcite and lesser amounts of sericite, magnetite and pyrite (Fig. 4i). In this zone, epidotization of feldspars and chloritization of ferromagnesian minerals and formation of calcite veinlets in rocks are the main alteration signatures. Besides, in altered ferromagnesian crystals, Ti-oxide aggregates and bladed sericite were also observed.

The silicic alteration zone outcropped in the eastern part of the area; barren silica-alunite cap has been preserved in an almost NE–SW trend as silicified ledges with a quartz-kaolinite halo around (Fig. 4j–l). This cap almost is observed in the transitional zone between porphyry and epithermal systems in the western part of the porphyry system.

Quartz veins

Based on the mineralogical studies and the relationship of veinlets, five main veinlets were identified which are associated with potassic, phyllic and silicic alterations, respectively: (i) A-type quartz veinlets (Qtz I) in potassic alteration zone (Fig. 6a), (ii) B-type quartz veinlets (Qtz II) in phyllic alteration zone, consisting of

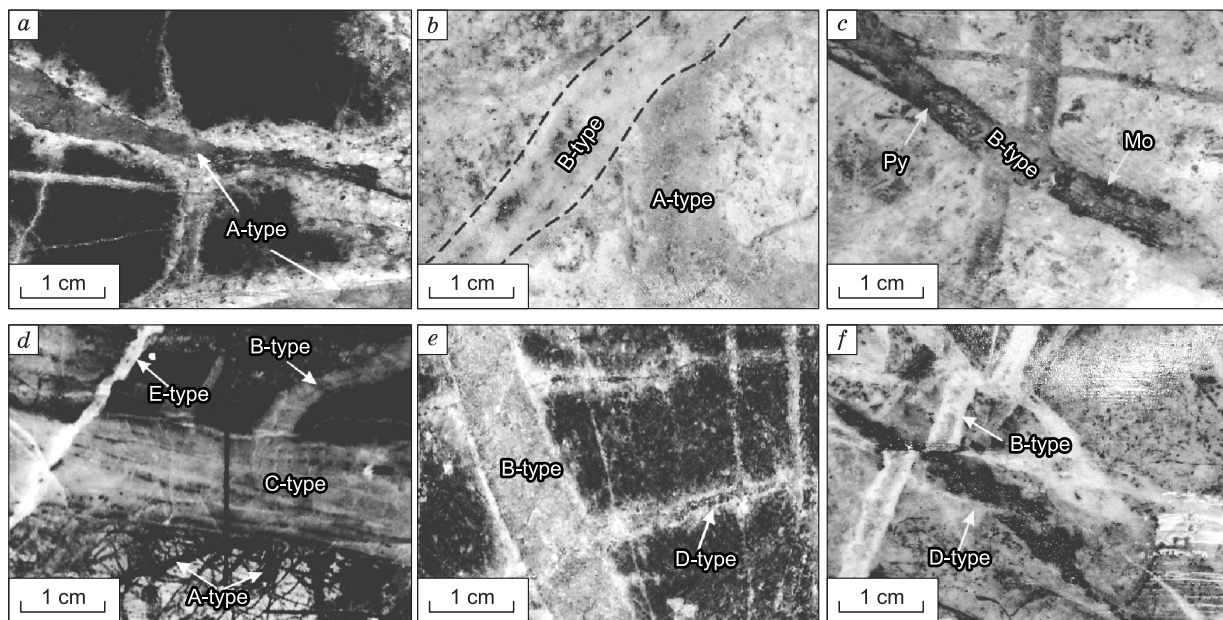


Fig. 6. Photographs of drill core samples and vein systems of different stages.

(a) A-type irregular veinlet with K-feldspar and biotite in context of potassic alteration; (b and c) B-type quartz veinlet cutting A-type in monzonite porphyry with phyllic alteration in context with copper and molybdenite mineralization; (d) dissection of B-type veinlet by C-type veinlet with sericite-silicic alteration in context and itself dissected by E-type veinlet; (e and f) B-type veinlet cut by D-type veinlet with sericite-silicic alteration in context. Mo, molybdenite; Py, pyrite.

Fig. 7. Stages of mineralization and the paragenetic sequence of minerals for the Kighal deposit.

quartz + pyrite + chalcocopyrite ± molybdenite (Fig. 6b, c) and also sulfide-carbonate veinlets with stockwork texture comprised by calcite, pyrite and minor amount of chalcocopyrite, sphalerite and galena, (iii) C-type quartz veinlets (Qtz III) are mainly pyritic, recognized in potassic and phyllic alteration zones (Fig. 6d), (iv) D-type quartz veinlets (Qtz IV) are anhydritic, containing small amounts of pyrite, observed in the border of the porphyry stock (Fig. 6e, f) and (v) E-type quartz veinlets (Qtz V) in silicic alteration zone (Fig. 6d) (Hassanpour, 2010; Hassanpour et al., 2015). These veinlets vary from ~0.5 mm to several mm in thickness. Quartz and sulfide minerals from the Qtz I, Qtz II and Qtz V veinlets display close association and intergrowth boundaries, being rich in fluid inclusion and were selected for microthermometric studies, while others have no suitable inclusions for this purpose. Figure 7 represents the paragenetic sequence and mineralization stages for the Kighal deposit.

Minerals	Pre-ore	Main-ore	Post-ore	Weathering
Biotite	████████			
Anhydrite	████████			
Quartz I	████████			
Quartz II		████████		
Sericite		████████		
Quartz III		████████		
Clay minerals		████████		
Albite		████████		
Chlorite		████████		
Epidote		████████		
Calcite		████████		
Quartz IV		████████		
Quartz V			████████	
Alunite			████████	
Magnetite	████████			
Pyrite	████████	████████	████████	
Molybdenite	████████			
Chalcocopyrite	████████	████████	████████	
Bornite		████████	████████	
Hematite		████████	████████	
Galena		████████		
Sphalerite		████████		
Covellite				████████
Malachite				████████
Azurite				████████
Goethite				████████
Limonite				████████

SAMPLES AND ANALYTICAL METHODS

In order to understand the physicochemical natures of the ore-forming fluids, the study of FIs were conducted on double-polished sections of the quartz crystals belong to quartz-pyrite veinlets and quartz-sulfide rich veinlets involved in the phyllic and potassic alteration zones from exploratory drill holes and surface outcrops in the Kighal deposit. FIs study was carried out at the Mineralogical Laboratory of the Advanced Research Center for Ore Materials in Karaj (Iran). In this study, the results of FIs data (Simmonds et al., 2015) were revised on ten double-polished sections (five samples of quartz-sulfide veinlets within the potassic and phyllic zones and five samples of quartz-sulfide veinlets within the phyllic zone). Eight samples from potassic and phyllic zones for petrography of FIs were studied by Olympus microscope, and microthermometry measurement was performed by THMS600 Lynkam and via heating and freezing at the Mineralographic Laboratory of the Advanced Research Center for Ore Materials in Karaj (Iran). The instrument accuracy when heating and freezing was ±0.1 °C and heating ranges are between -180 and +600 °C. The instrument is equipped with two TP94 heating and LNP cooling controller, nitrogen tank (to pump nitrogen for freezing) and water tank (for cooling at high temperatures). For two-phase halite-bearing FIs, the transitional temperature including homogenization temperatures of liquid-vapor phase or Th(LV) and the temperature of halite dissolution Th(NaCl) was determined and the presence of trapped chemical species NaCl, KCl in the fluids was estimated based on the eutectic temperature (T_e). The density of FIs is calculated according to Zhang and Frantz (1987).

To study oxygen and hydrogen isotopic composition, five samples of the hydrothermal biotite from potassic alteration and ten samples of sericite and two quartz samples from the phyllic alteration zone, were grinded to 20 meshes, washed by distilled water and separated by binocular microscope and were analyzed at Queen's University in Canada. Finally, for whole rock geochemical analysis (Table 1), twenty samples were collected from the surface and from the least altered rocks in the Kighal area. After grinding in the size of 200 meshes, were analyzed by ICP-MS at the Amdel Laboratory in Australia.

RESULTS

Geochemistry

In the diagram of Cox et al. (1979), the rocks are classified as dacite, trachyandesite, trachyte and rhyolite (Fig. 8a). The selected magmatic rock samples from Kighal plot within the calc-alkaline field in the diagrams

Table 1. Bulk-rock chemical composition (major and trace elements) of selected rock samples in the Kighal area

Component	Gd	Gd	Gd	Gd	Gd	Di	Gb.d	Rh	And	And	And	And	And	And	And	Da	Da	Da	Tr	Tr.a
SiO ₂	62.64	57.41	59.36	58.92	63.71	59.60	47.25	67.98	71.33	62.94	62.52	46.42	50.07	52.06	56.79	61.18	61.70	62.11	59.19	58.67
TiO ₂	0.57	0.62	0.68	0.67	0.50	0.67	1.92	0.32	0.42	0.45	0.60	2.15	1.37	0.93	1.12	0.67	0.65	0.67	0.88	0.90
Al ₂ O ₃	14.62	15.06	15.07	14.32	15.26	15.81	15.45	17.44	13.81	17.89	15.58	14.62	15.47	20.02	15.30	16.25	15.60	16.11	15.92	17.64
Fe ₂ O ₃	2.11	3.00	2.22	2.38	1.67	2.42	5.06	1.06	1.31	1.37	2.02	3.78	3.17	3.23	2.63	2.23	2.69	2.64	2.67	2.17
FeO ₁	2.48	4.64	2.90	2.45	1.76	2.72	6.70	1.14	1.23	1.57	2.29	6.49	5.19	3.98	2.86	2.58	2.79	2.75	3.02	2.69
MnO	0.08	0.12	0.08	0.09	0.07	0.09	0.21	0.02	0.04	0.03	0.18	0.15	0.13	0.20	0.06	0.08	0.11	0.11	0.11	0.07
MgO	2.17	1.82	2.32	2.98	1.34	2.59	6.07	0.35	0.22	1.16	1.18	6.07	7.79	2.22	3.27	2.54	1.48	1.48	1.96	2.79
CaO	4.83	4.50	5.29	5.20	4.46	5.48	7.93	4.15	2.59	6.90	5.55	9.99	9.19	7.78	6.13	5.54	5.11	5.26	6.30	6.70
Na ₂ O	3.83	2.87	3.23	3.64	3.21	3.34	4.83	4.99	3.73	5.07	3.96	3.65	3.98	3.95	2.71	4.11	3.94	3.99	4.69	4.95
K ₂ O	2.41	1.43	2.07	2.69	3.40	2.66	0.10	1.42	2.88	1.22	2.70	1.70	1.28	2.11	5.19	2.29	3.59	3.63	2.42	1.55
P ₂ O ₅	0.24	0.12	0.27	0.35	0.22	0.27	0.33	0.16	0.18	0.29	0.28	0.93	0.56	0.15	0.55	0.28	0.29	0.29	0.52	0.48
LOI	1.84	5.36	5.66	4.84	5.52	4.43	4.53	0.96	0.78	1.50	1.99	1.03	1.04	4.48	4.90	3.84	0.07	0.38	1.28	1.53
Total	98.10	97.58	99.49	98.83	101.29	100.43	101.34	100.03	98.58	100.50	99.12	97.76	99.86	101.65	101.83	101.91	98.40	99.78	99.34	100.42
Ba	812	250	751	922	1150	1150	39.9	511	784	411	1050	1120	492	452	1360	1730	916	878	793	675
Rb	58	48	50.2	55.6	79.2	61.4	3.4	33.4	96.8	20.8	90.2	22.6	23.2	38.4	97.8	48	121	117	58.6	35.6
Sr	624	334	524	781	403	684	159	723	395	1010	581	1270	941	402	1080	763	681	672	864	1010
Cs	0.7	5.3	1.5	1.2	2.6	2.1	2.3	0.3	1.4	0.2	1.1	0.7	0.3	1.7	2.6	1.8	1.4	1.3	1.3	0.9
Li	13	20	12	11.5	5	12	13.5	13	8.5	7.5	9	8.5	12	23	18	15	11.5	13.5	9.5	7
Tl	0.4	0.5	0.3	0.4	0.5	0.5	<0.1	<0.1	0.3	<0.1	0.3	0.2	<0.1	0.3	0.6	0.3	0.2	0.2	0.1	0.2
Nb	10	4.5	10.5	13.5	11.5	11	9.5	7.5	18	9.5	27	27.5	21	4.5	24	13	24.5	24.5	19	23
Hf	1.8	2.4	2.2	1.8	1.5	2	2.7	2	3.5	1.9	3.3	3.7	3.1	2.4	3.6	1.8	3.3	3.1	3.3	3.3
Zr	61	99	86	72	59	73	74	87	155	86	150	200	158	94	147	62	125	120	164	168
Y	12.9	17.9	13.2	14.2	10.2	14.6	34.9	4	16.1	4	18.8	21.8	16.4	22.6	13	12.6	23.5	21.3	17.8	10.7
Th	11.8	2.4	9.3	15.9	15.2	11.3	0.7	3.6	13.4	5.5	11.1	8.7	8.9	2.5	22.8	12.4	20.4	20	12.1	7.9
U	3.6	0.4	2.5	4.8	5.5	3.6	0.1	1.3	4.4	1.2	4	1.8	2	0.9	6.7	4.2	4.7	4.3	3.3	1.5
Ni	19	6	30	35	19	28	55	8	4	11	4	57	175	11	86	30	4	4	16	23
Co	12.8	25.2	17.7	15.9	8.5	14.1	36.8	4.6	4	7.4	7.4	35.1	39.3	22.7	18.5	13.8	10.8	10.5	16.7	15.1
Sc	8.5	16.5	11.5	9.5	7.5	10.5	35.5	3.5	4	5.5	6	21	19	24	12	9	8	8.5	10.5	9.5
Pb	11	4	12	16	17	11	5	9	16	7	11	7	8	5	23	13	18	16	15	9
Bi	<0.1	<0.1	<0.1	0.1	<0.1	<0.1	<0.1	<0.1	<0.1	<0.1	<0.1	<0.1	<0.1	<0.1	<0.1	<0.1	<0.1	<0.1	<0.1	<0.1
La	28.1	9.3	29.7	50.1	34.4	29.7	14	13.2	30.4	22.2	47.5	57	45.1	9.6	63.6	36.3	58.5	55.4	44.2	37.6
Ce	49.7	19.7	51.6	85	61.2	53	33.1	19	51.4	36.3	83	115	80.4	20.4	114	63.6	102	98.1	79.1	65.7
Pr	5.9	2.55	6.3	8.6	6.2	6.1	5.3	2.5	5.55	4	9.45	13.3	9	2.7	11.7	7.15	11.6	11.4	8.65	7.25
Nd	19.3	10.8	21.8	28.6	19.7	20.5	23.7	8.42	18.2	13.4	31.3	48.6	30.5	11.4	37.9	23.5	40.5	39	30	24.5
Sm	3.54	2.84	4.22	4.78	3.16	3.84	6.4	1.58	3.24	2.24	5.64	8.62	5.48	3.1	5.8	4.22	7.4	7.38	5.5	4.32
Eu	1.12	0.94	1.3	1.4	0.94	1.2	1.98	0.54	0.96	0.76	1.7	2.6	1.68	1.14	1.58	1.28	2.06	2.04	1.58	1.36
Gd	2.75	2.95	3.3	3.25	2.2	2.9	6.9	1.2	2.6	1.4	3.95	6.05	3.85	3.2	3.5	3.1	5.45	5.5	4	2.9
Tb	0.38	0.48	0.46	0.42	0.28	0.4	1.16	0.14	0.38	0.16	0.54	0.72	0.5	0.54	0.44	0.42	0.72	0.7	0.5	0.36
Dy	2.46	3.38	2.84	2.6	1.76	2.56	6.88	0.74	2.52	0.88	3.38	4.2	3.08	3.74	2.44	2.56	4.32	4.32	3.06	2.12
Ho	0.44	0.66	0.52	0.44	0.32	0.44	1.46	0.12	0.46	0.12	0.58	0.66	0.52	0.72	0.42	0.42	0.74	0.74	0.5	0.34
Er	1.25	1.9	1.4	1.15	0.8	1.2	3.9	0.3	1.35	0.3	1.55	1.65	1.35	2.1	1.05	1.15	1.9	1.95	1.35	0.85
Tm	0.2	0.3	0.2	0.15	0.1	0.2	0.55	<0.05	0.2	<0.05	0.25	0.2	0.2	0.3	0.15	0.15	0.25	0.25	0.2	0.1
Yb	1.2	1.8	1.25	1.05	0.85	1.05	3.3	0.25	1.45	0.25	1.45	1.25	1.15	2.1	0.85	1	1.8	1.8	1.15	0.7
Lu	0.18	0.3	0.2	0.16	0.12	0.18	0.46	0.04	0.22	0.04	0.22	0.18	0.18	0.3	0.14	0.16	0.26	0.28	0.18	0.1

Note. Gd, granodiorite; Di, diorite; Gb.d, gabbrodiorite; Rh, rhyolite; And, andesite; Da, dacite; Tr, trachyte, Tr.a, trachyandesite.

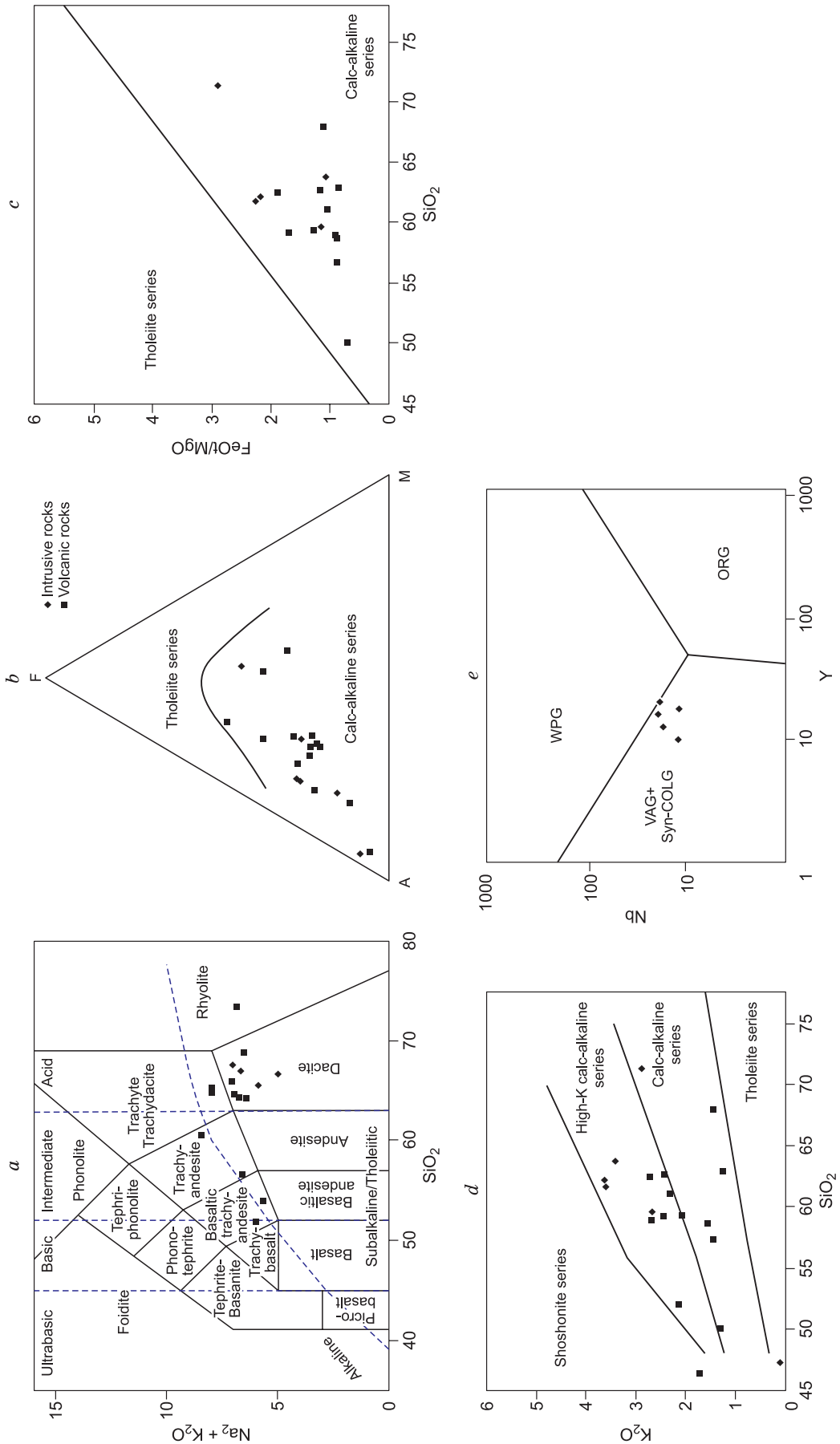


Fig. 8. (a) Position of the selected rock in the diagram of Cox et al. (1979), plotting in the range of as dacite, trachyandesite, trachyte and rhyolite; (b, c) location of the selected rock samples in the diagrams of Irvine and Baragar (1971) and Miyashiro (1974) both showing calc-alkaline series; (d) the selected rock samples plot in the high-K calc-alkaline to calc-alkaline series (Pecceirillo and Taylor, 1976); (e) tectonic setting of the samples, shows ranging from continental arc and syncollisional (Pearce et al., 1984).

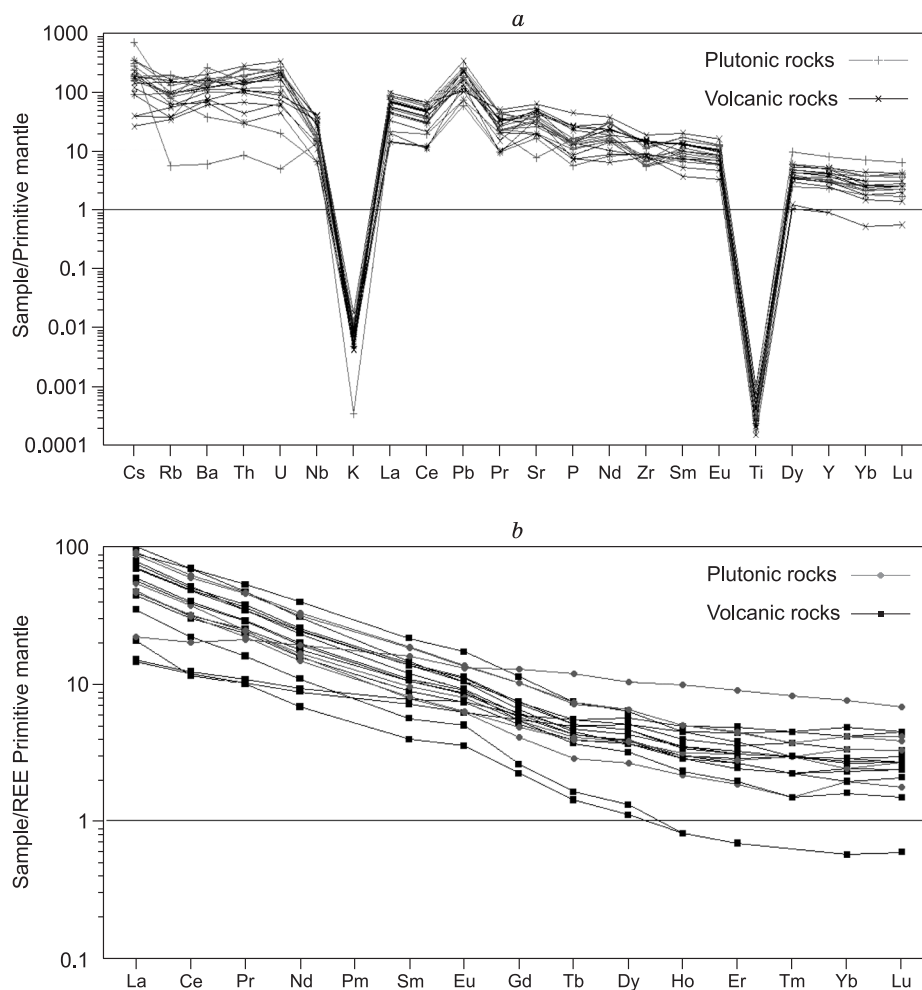


Fig. 9. (a) Primitive mantle-normalized incompatible element distribution spidergrams for the igneous suite from the Kighal area; (b) chondrite-normalized REE patterns for the igneous suite from the Kighal area (Sun and McDonough, 1989).

of SiO_2 vs. FeO/MgO diagram of Miyashiro (1974) (Fig. 8b) and Irvine and Baragar (1971) (Fig. 8c). In the diagram of Peccerillo and Taylor (1976) (Fig. 8d), the data plot in the calc-alkaline to high-K calc-alkaline fields. In the diagram of Pearce et al. (1984) for discrimination of tectonic setting, the samples plot in the orogeny and granitoid related to volcanic arc (Fig. 8e). In Fig. 9a, the intrusive and subvolcanic samples separately normalized in one group of volcanic samples and in another group with the primitive mantle, indicating that all samples are enriched in LILE such as Y, Th, Ba, Rb and Cs, which can be due to contamination of the mantle wedge with crust, sediments and surface material resulting from the transfer by subducted oceanic crust (Tatsumi et al., 1986; Davidson et al., 1996; De Hoog et al., 2001). However, in this diagram depletion of HFSEs such as Ti and Nb is significant because of the immobility nature of these elements in a subduction zone, they do not participate in the partial melting process and thus, in the produced magma from the mantle wedge, depletion of these elements is expected. This characteristic is especially attributed to subduction zones (Brenan et al., 1994; Foley et al., 2000) (Fig. 9B).

Both the plutonic and volcanic rocks from the Kighal area display LREE-enriched patterns with respect to HREE (Fig. 9b), as indicated by $(\text{La}/\text{Yb})_n$ of 3.04–63.69 and $(\text{Tb}/\text{Yb})_n$ of 1.16–2.9 (Table 1) and show sub-horizontal MREE and HREE patterns. The volcanic rocks show relatively lower contents of REE than those of the plutonic rocks. The LREE enriched patterns (Fig. 9b), with $(\text{La}/\text{Yb})_n$ ratios of 3.04–63.69, are similar to the geochemical features of magmatic rocks generated in volcanic arc setting (Shimizu et al., 1992; Wyman, 1999).

Fluid inclusions studies

Fluid inclusion petrography. In order to estimate the formation temperatures of the deposit, the fluid inclusion assemblage (FIA) method was applied on quartz samples from the early-, middle- and late-stages,

including Qtz I, Qtz II and Qtz V, respectively. Quartz crystals in a variety of the mineralized quartz veinlets in the potassic, phyllic and silicic alteration zones are rich in primary FIs with size up to 20 μm , which show irregular, elongated and rounded shapes according to Roedder (1984) and Shepherd et al. (1985). Based on the frequency, nature and content of the FIs phases at room temperature, three groups of FIs have been identified in the Kighal deposit: (1) liquid-rich (LV) (Fig. 10a, c, e), (2) vapor-rich (VL) (Fig. 10b), and (3) multiphase LVS (Fig. 10d). In addition to, a few single-phase liquid and vapor-rich CO_2 -bearing fluids were observed in the quartz-pyrite and quartz-sulfide veinlets from potassic and phyllic alteration zones.

Most vapor-rich inclusions from relatively thin quartz-sulfide veinlets in the potassic zone are very small (<5 μm), thus they are not suitable for microthermometry study. Moreover, the samples from the anhydrite/gypsum veinlets and carbonate veinlets, are not suitable for microthermometry study. In this study, FIs microthermometry was conducted on primary LV, VL and multiphase LVS FIs (Fig. 10) as well as several data modified after Simmonds et al. (2015). Degree filling of the inclusions is about 0.7 to 0.8. Two-phase LV FIs ($L > V$; sizes between 6 and 16 μm) during the heating, homogenized to liquid and are present in all vein types of the deposit, but are dominant in the unmineralized surficial quartz-pyrite veinlets of the phyllic alteration zone. Many multiphase LVS FIs sizes range between 7 and 25 μm and solid phases such as halite, hematite, sylvite, opaque minerals (chalcopyrite) and anhydrite were observed in these FIs (Simmonds et al., 2015).

Based on petrographic observations, daughter solid phases in FIs have shown that fluids are involved in high metal concentrations. The presence of opaque daughter and chalcopyrite phases in FIs as well as the presence of these minerals within quartz veinlets confirmed that these inclusions were involved in the ore-bearing fluids. Since hematite within quartz veinlets is not seen, the presence of the daughter hematite within studied inclusions may be due to the hydrogen diffusion after trapping through the inclusions boundaries with a high level of FeCl_2 (Roedder, 1984; Mavrogenes and Bodnar, 1994; Wilkinson, 2001).

Fluid inclusions microthermometry. The results of homogenization temperature and salinity determination in different stages of the mineralization are presented in Table 2 and also illustrated in Figs. 11 and 12. Seventy-one fluid inclusions were studied in three groups of two-phase liquid-rich, two-phase vapor-rich and multiphases FIs in different stages of the mineralization within coarse-grained quartz crystals (Fig. 11a-f). The majority of FIs homogenized to liquid.

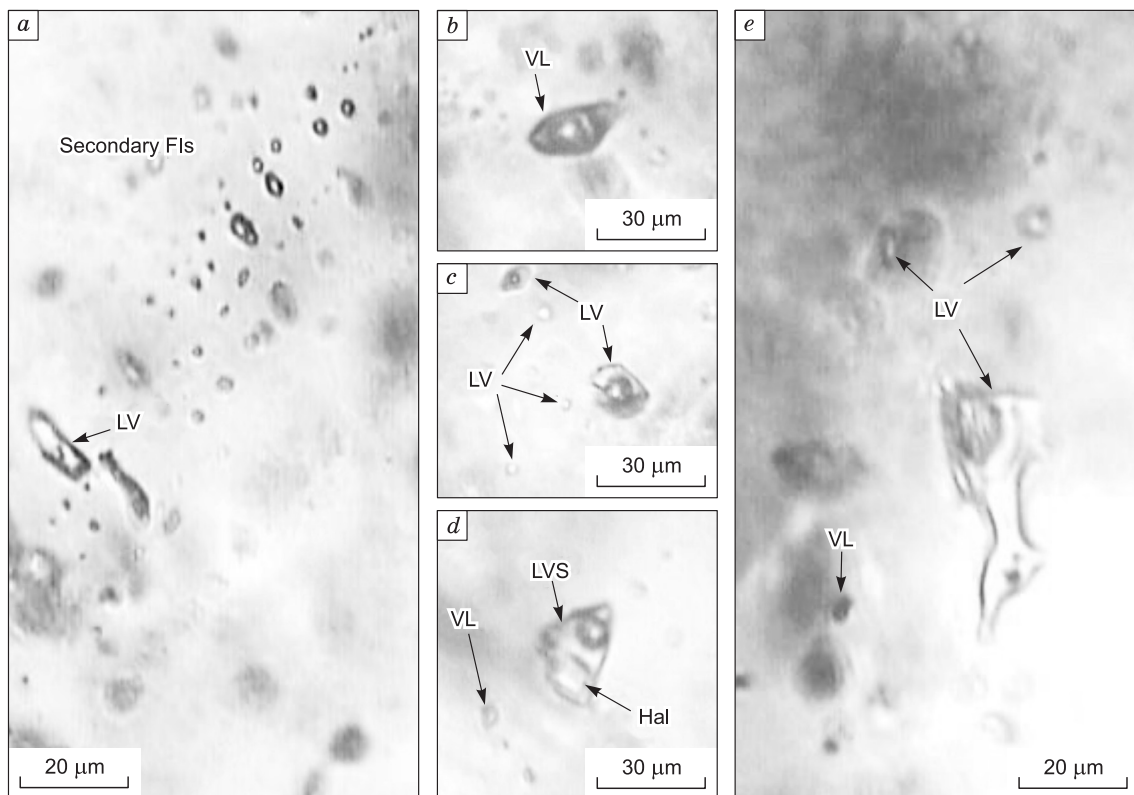


Fig. 10. Fluid inclusion types and fluid inclusion assemblages from the Kighal deposit.

(a) Several secondary liquid-rich (LV) fluid inclusions; (b) primary vapor-rich (VL) fluid inclusion assemblage showing boiling condition; (c) primary liquid-rich (LV) fluid inclusion assemblage; (d) primary multiphase (LVS) fluid inclusion with clearly visible halite daughter crystals; (e) the coexistence of primary vapor-rich and liquid-rich fluid inclusion assemblages showing boiling condition.

Table 2. Microthermometric data of fluid inclusions in different stages of quartz samples from the Kighal deposit

No.	Zone	Vein type	Size, μm	Origin	Type	Te, $^{\circ}\text{C}$	Tm, $^{\circ}\text{C}$	Th, $^{\circ}\text{C}$	Th _{Halite} , $^{\circ}\text{C}$	Salinity, wt.% NaCl-equiv.	Density, gr/cm^3
1	Potassic	Qtz I	8	P	LVS	-43	-17.1	420	360	43.35	
2	Potassic	Qtz I	20	P	LVS	-45	-18.3	384	500	59.76	
3	Potassic	Qtz I	14.5	P	LVS	-51	-16.1	330	410	48.55	
4	Potassic	Qtz I	18	P	LVS	-49	-16.5	345	166	39.52	0.75
5	Potassic	Qtz I	12	P	LVS	-52	-14.9	450	280	36.68	0.54
6	Potassic	Qtz I	6	P	LVS	-52	-18.2	375	461	54.64	0.68
7	Potassic	Qtz I	9	P	LVS	-52	-16.2	352	356	49.11	0.7
8	Potassic	Qtz I	11	P	LVS	-52	-17.9	390.9	320	39.76	0.78
9	Potassic	Qtz I	14	P	LVS	-52	-15.8	358	285	37.04	0.76
10	Potassic	Qtz I	9	P	LVS	-39	-15.2	374	317	36.19	
11	Potassic	Qtz I	12	P	LVS	-49	-15.4	361	280	36.68	
12	Potassic	Qtz I	7	P	LVS	-53	-18.4	330	320	39.76	
13	Potassic	Qtz I	14	P	LVS	-57	-15.4	293	254	45.33	
14	Potassic	Qtz I	12	P	LVS	-44	-18.7	310	425	54.83	
15	Potassic	Qtz I	7	P	LVS	-45	-16.7	265	362	43.54	
16	Potassic	Qtz I	8	P	LVS	-58	-20.2	380	450	53.26	
17	Potassic	Qtz I	12	P	LVS	-49	-18.3	403.3	350	42.4	
18	Potassic	Qtz I	8	P	LV	-39	-1.5	185		2.56	0.9
19	Potassic	Qtz I	6	P	LV	-36	-2.2	188		3.69	0.91
20	Potassic	Qtz I	8	P	LV	-33	-2	208		3.37	0.88
21	Phyllic	Qtz II	6	P	LV	-39	-7	284.5		10.51	0.86
22	Phyllic	Qtz II	6	P	LV	-39	-3.3	244		5.4	0.86
23	Phyllic	Qtz II	6	P	LV	-35	-7.5	238		11.13	0.92
24	Phyllic	Qtz II	6	P	LV	-39	-6.4	228		9.75	0.92
25	Phyllic	Qtz II	7	P	LV	-39	-4.5	273		7.16	0.84
26	Phyllic	Qtz II	6	P	LV	-35	-7	296.1		10.51	0.84
27	Phyllic	Qtz II	7	P	LV	-45	-4	303		6.44	0.78
28	Phyllic	Qtz II	5	P	LV	-45	-3	280.5		4.94	0.8
29	Phyllic	Qtz II	25	P	LV	-43	-0.6	225		1.1	
30	Phyllic	Qtz II	25	P	LV	-38	-0.6	199		1.1	
31	Phyllic	Qtz II	5	P	LV	-42	-0.4	258		0.7	
32	Phyllic	Qtz II	5	P	LV	-42	-0.5	292		0.9	
33	Phyllic	Qtz II	20	P	LV	-39	-0.5	266		0.9	
34	Phyllic	Qtz II	20	P	LV	-49	-0.7	208		1.2	
35	Phyllic	Qtz II	5	P	LV	-44	-0.7	185		1.2	
36	Phyllic	Qtz II	5	P	LV	-47	-0.7	185		1.2	
37	Phyllic	Qtz II	25	P	LV	-43	-0.4	269		0.7	
38	Phyllic	Qtz II	20	P	LV	-45	-0.7	363		1.2	
39	Phyllic	Qtz II	5	P	LV	-48	-0.6	196		1.1	
40	Phyllic	Qtz II	5	P	LV	-38	-0.6	196		1.1	
41	Phyllic	Qtz II	5	P	LV	-47	-0.6	284		1.1	
42	Phyllic	Qtz II	25	P	LV	-47	-0.4	245		0.7	
43	Phyllic	Qtz II	7.5	P	LV	-38	-0.4	264		0.7	
44	Phyllic	Qtz II	7.5	P	LV	-39	-0.5	188		0.9	
45	Phyllic	Qtz II	20	P	LV	-52	-0.9	163		1.6	
46	Phyllic	Qtz II	20	P	LV	-49	-0.3	171		0.5	
47	Phyllic	Qtz II	5	P	LV	-44	-0.8	187		1.4	
48	Phyllic	Qtz II	30	P	LV	-39	-1.3	191		2.2	

(continued on next page)

Table 2 (continued)

No.	Zone	Vein type	Size, μm	Origin	Type	Te, $^{\circ}\text{C}$	Tm, $^{\circ}\text{C}$	Th, $^{\circ}\text{C}$	Th _{Halite} , $^{\circ}\text{C}$	Salinity, wt.% NaCl-equiv.	Density, gr/cm^3
49	Phyllic	Qtz II	8	P	VL	-32	-0.5	339		0.8	
50	Phyllic	Qtz II	7	P	VL	-35	-0.3	466		0.5	
51	Phyllic	Qtz II	6	P	VL	-31	-0.2	358.5		0.3	
52	Phyllic	Qtz II	8	P	VL	-41	-0.4	334.5		0.7	
53	Phyllic	Qtz II	10	P	VL	-32	-0.2	430		0.3	
54	Phyllic	Qtz II	12	P	VL	-37	-0.3	423		0.5	
55	Silicic	Qtz V	9	P	LV	-41	-5	224		2.87	0.9
56	Silicic	Qtz V	8	P	LV	-45	-5	282		1.87	0.83
57	Silicic	Qtz V	6	P	LV	-41	-2	283		3.37	0.77
58	Silicic	Qtz V	16	P	LV	-41	-3.5	289		5.7	0.79
59	Silicic	Qtz V	7	P	LV	-39	-4.5	275		2.16	0.83
60	Silicic	Qtz V	7	P	LV	-39	-1.5	293		2.56	0.74
61	Silicic	Qtz V	7	P	LV	-41	-1.5	280		2.56	0.77
62	Silicic	Qtz V	11	P	LV	-41	-1.5	294		2.56	0.74
63	Silicic	Qtz V	12	P	LV	-49	-0.7	228		1.22	0.84
64	Silicic	Qtz V	5	P	LV	-49	-1.5	235		2.56	0.84
65	Silicic	Qtz V	8	P	LV	-52	-1.5	228		2.56	0.85
66	Silicic	Qtz V	8	P	LV	-54	-1.2	224		2.06	0.85
67	Silicic	Qtz V	11	P	LV	-52	-0.8	230		1.39	0.84
68	Silicic	Qtz V	11	P	LV	-49	-0.6	228		1.05	0.84
69	Silicic	Qtz V	13	P	LV	-49	-1	218		1.73	0.86
70	Silicic	Qtz V	5	P	LV	-45	-0.7	226		1.22	0.84
71	Silicic	Qtz V	6	P	LV	-49	-0.7	215		1.22	0.86

Table 3. Oxygen and hydrogen isotopic compositions in biotite, sericite and quartz (‰ SMOW), and calculated hydrothermal fluid compositions

Sample code	Alteration	Mineral	Th, $^{\circ}\text{C}$	$\delta^{18}\text{O}_{(\text{VSMOW})}$	$\delta\text{D}_{(\text{VSMOW})}$	$\delta^{18}\text{O}_{(\text{H}_2\text{O})}$	$\delta\text{D}_{(\text{H}_2\text{O})}$	
SH-51	Potassic	Biotite	350	3	-82	4.7	-24.3	This study
SH-134	Potassic	Biotite	350	2.3	-84	4	-26.3	This study
SH-288	Potassic	Biotite	350	3.7	-86	5.4	-28.3	This study
SH-281	Potassic	Biotite	350	3.5	-83	5.2	-25.3	This study
SH-289	Potassic	Biotite	350	3.4	-89	5.1	-31.3	This study
SH-122	Phyllic	Sericite	270	9	-69	6.9	-13.2	This study
SH-128	Phyllic	Sericite	270	8	-72	5.9	-16.2	This study
SH-135	Phyllic	Sericite	270	7.5	-85	5.4	-29.2	This study
SH-141	Phyllic	Sericite	270	9.9	-71	7.8	-15.2	This study
SH-145	Phyllic	Sericite	270	8.9	-67	6.8	-11.2	This study
SH-147	Phyllic	Sericite	270	9.3	-67	7.2	-11.2	This study
SH-278	Phyllic	Sericite	270	10.5	-68	8.4	-12.2	This study
SH-287	Phyllic	Sericite	270	6.4	-68	4.3	-12.2	This study
SH-391	Phyllic	Sericite	270	9.4	-73	7.3	-17.2	This study
SH-518	Phyllic	Sericite	270	9.2	-68	7.1	-12.2	This study
SH-393	Qtz-Alu	Quartz	250	12.7	-62	3.3	-62	This study
SH-282	Qtz-Alu	Quartz	250	8	-74	-1.4	-74	This study
A1		Quartz		8.9	-61	5.4	-61	(Simmonds et al., 2015)
B1		Quartz		8.9	-63	5.8	-63	(Simmonds et al., 2015)
B2		Quartz		8.1	-77	5.7	-77	(Simmonds et al., 2015)

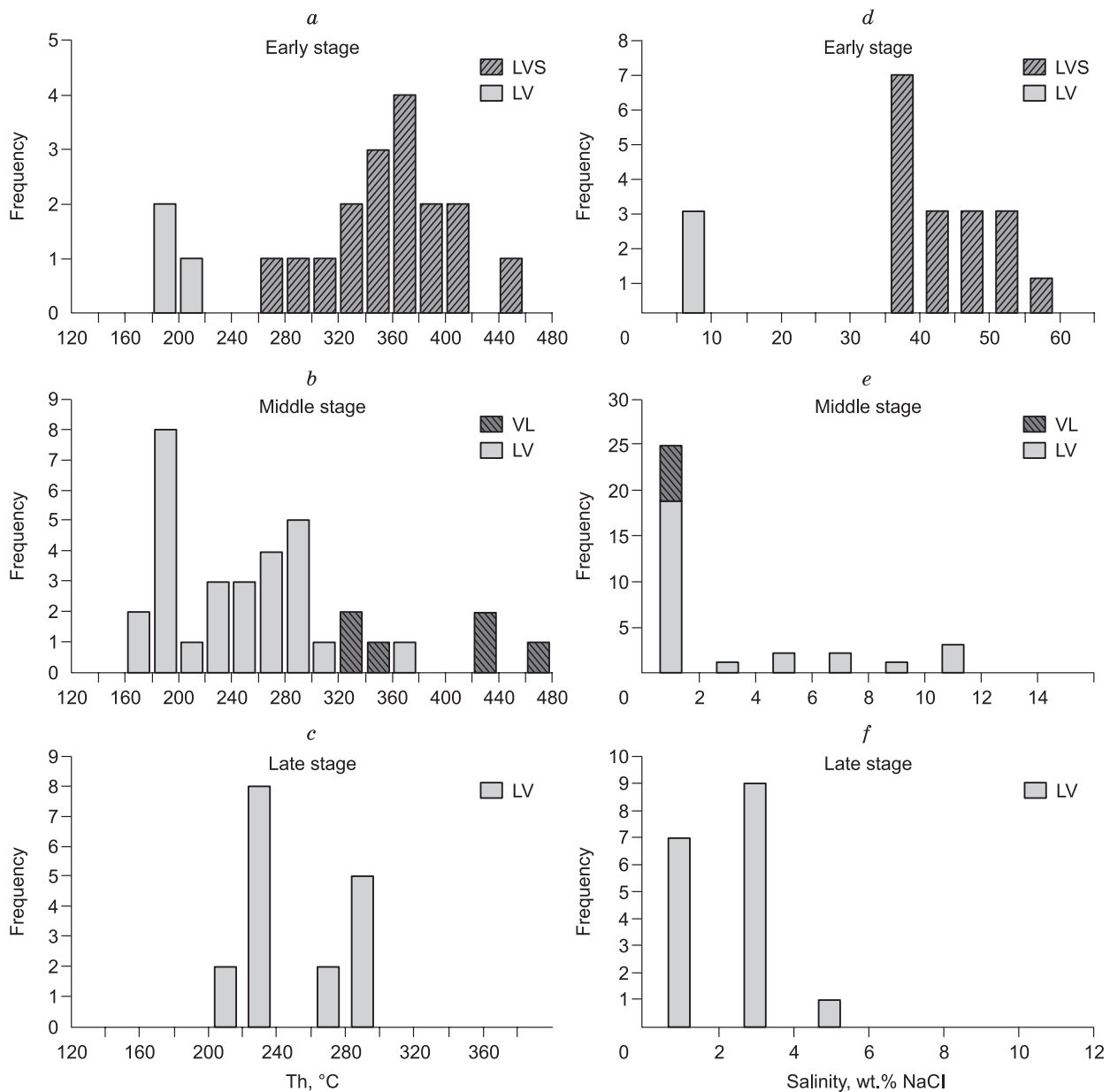


Fig. 11. Histograms showing homogenization temperatures and salinities of primary two-phase and multiphase fluid inclusions assemblages in different stages of mineralization.

Early stage. Twenty fluid inclusions (7 FIAs) were studied in coarse-grained quartz I crystals. The homogenization temperature for primary LV FIAs ranges from 185–208 °C (average 194 °C; $n = 3$) and from 265 to 450 °C (average 360 °C; $n = 17$) for multiphase inclusions homogenized by halite dissolution ($[Th_{(NaCl)}]$) (Table 2, Fig. 11a). The measured initial melting (T_m) in primary liquid-rich inclusions (LV) in quartz I ranges from –33 and –54 °C, indicating halite is the main phase in the solution and the existence of $NaCl-CaCl_2 \pm FeCl_2 \pm MgCl_2$ in the ore-forming fluids (Table 2) (Roedder, 1984; Shepherd et al., 1985). The values of temperature of ice melting ($T_{m,ice}$) from primary LV FIAs range between –2.2 and –1.5 °C and correspond to a salinity of 2.5–3.7 wt.% NaCl-equiv. (average 3.2 wt.% NaCl-equiv.). The salinity of LVS FIAs was calculated using the melting temperature of halite daughter (i.e., $Th_{(NaCl)}$) (Simmonds et al., 2015). The maximum salinity belongs to multiphase LVS FIAs range from 36 to 59 wt.% NaCl-equiv. (average 44 wt.% NaCl-equiv.) (Table 2, Fig. 11d).

Middle stage. Thirty-four fluid inclusions (7 FIAs) were studied in coarse-grained quartz II crystals. The homogenization temperature (Th) in primary LV FIAs ranges from 163 to 363 °C (average 238 °C; $n = 28$) and from 334 to 466 °C (average 391 °C; $n = 6$) in primary VL FIAs (Table 2, Fig. 11b). The measured initial melt-

Table 4.

Pb-isotopes from the Kighal deposit

Code	$^{206}\text{Pb}/^{204}\text{Pb}$	$^{207}\text{Pb}/^{204}\text{Pb}$	$^{208}\text{Pb}/^{204}\text{Pb}$	$^{232}\text{Th}/^{208}\text{Pb}$	^{206}Pb	^{207}Pb	^{208}Pb
Kg34	18.81603	15.61169	38.91772	110.1816021	0.001666	0.001999	0.000798
Kg45	18.79547	15.63517	38.88387	78.38773186	0.00139	0.001662	0.000665
Kg26	18.84006	15.63143	38.924	120.7673717	0.000648	0.000777	0.00031
Kg38	18.81104	15.60462	38.89944	87.00565684	0.001851	0.002221	0.000887
Kg23	18.75077	15.61888	38.83513	85.31711693	0.000835	0.000997	0.000399
Kg64	18.6734	15.6696	39.0629	92.185832	0.00103	0.00122	0.00049

ing obtained in LV inclusions is between -33 and -52 °C (average -41 °C) and in VL inclusions between -41 and -31 °C (average -34 °C) (Table 2). The temperatures of ice melting in LV inclusions are between -7.5 and -0.3 °C, corresponding to a salinity ranging from 0.5 to 11 wt.% NaCl-equiv. (average 3.1 wt.% NaCl-equiv.), whereas those in VL inclusions range from -0.5 to -0.2 °C which corresponds to a salinity range of 0.3–0.8 wt.% NaCl-equiv. (average 0.5 wt.% NaCl-equiv.) (Table 2, Fig. 11e).

Late stage. A total of 17 LV fluid inclusions (5 FIAs) were studied in coarse-grained quartz V crystals (E-type veinlet). The homogenization temperature (Th) shows a range from 215 to 294 °C (average 250 °C) (Table 2, Fig. 11c). The measured initial melting temperatures are between -54.0 and -39 °C (average -45 °C) (Table 2). The final temperature of ice melting ranges from -5 to -0.6 °C, corresponding to a salinity range of 1.0–5.7 wt.% NaCl-equiv. (average 2.3 wt.% NaCl-equiv.) (Table 2, Fig. 11f).

Oxygen and hydrogen isotopes

The results of the hydrogen and oxygen isotopic compositions for biotite, sericite and quartz are presented in Table 3. The fluid isotopic compositions ($\delta^{18}\text{O}_{\text{fluid}}$) were calculated using the mean value of the homogenization temperatures of fluid inclusion data obtained from this study. Biotite samples show $\delta^{18}\text{O}$ values ranging from 2.3 to 3.7‰ (average 3.1‰; $n = 5$) and also their δD values are between -89 and -82 ‰ (average -87 ‰; $n = 5$). The calculated $\delta^{18}\text{O}$ values of the fluid in equilibrium with biotite are between 4 and 5.4‰ (Table 3) (Zheng, 1993). Sericite samples show $\delta^{18}\text{O}$ values between 6.4 and 10.5‰ (average 8.8‰; $n = 10$) and δD between -85 and -67 ‰ (average -70.8 ‰; $n = 10$) (Table 3). The calculated isotopic compositions of the fluid in equilibrium with sericite show $\delta\text{D}_{\text{H}_2\text{O}}$ values of -29.25 to -11.2 ‰ (Suzuoki and Epstein, 1976) and $\delta^{18}\text{O}_{\text{H}_2\text{O}}$ values of 4.3 to 8.4‰ (Zheng, 1993). The $\delta^{18}\text{O}$ and δD values of quartz samples are between 8.0 and 12.7‰ (average 10.3‰; $n = 2$) and -74 and -62 ‰ (average -68 ‰; $n = 2$), and their calculated $\delta^{18}\text{O}$ of the fluid in equilibrium with quartz range from -1.4 to 3.3‰ (Table 3) (Zhang et al., 1989).

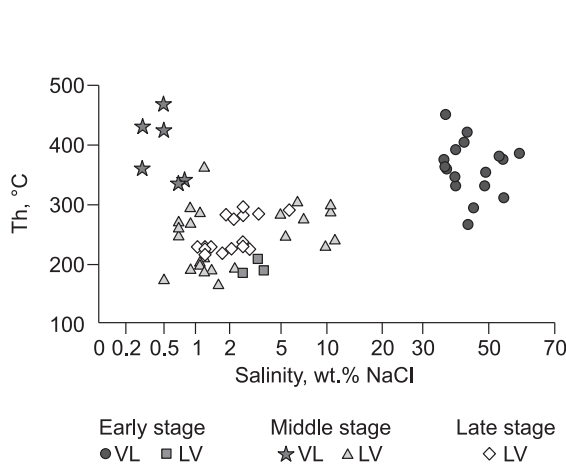


Fig. 12. Histograms of homogenization temperature vs. of salinity in wt.% NaCl-equiv. of primary fluid inclusions in different stages.

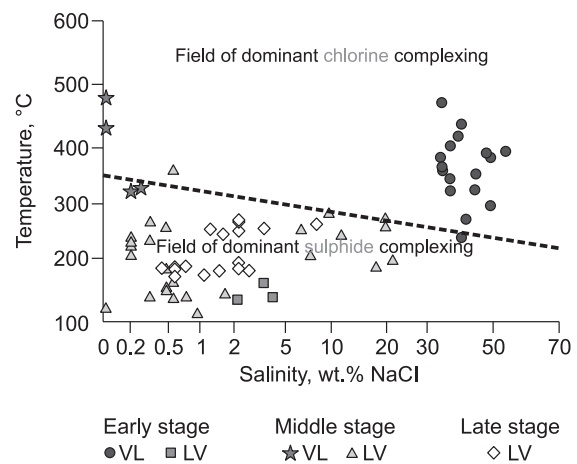


Fig. 13. Th-salinity diagram of fluids for determining the effective complex (anion) transporting elements (Pirajno, 2009).

Based on this diagram, HS^- , SO_4^{2-} , Cl^- and HCl^- complexes play an important role in the Kighal deposit.

DISCUSSION

Fluid evolution based on fluid inclusion data

According to microthermometry results, quartz-sulfide veinlets in the potassic alteration zones in deeper parts are found to have higher homogenization temperatures than the surficial barren quartz-pyrite veinlets. Generally, the wide ranges of salinity and homogenization temperature for multiphase and or two-phase FIs in quartz-sulfide veinlets from the potassic and phyllic alteration zones in the Kighal deposit are similar to other porphyry copper deposits (Etminan, 1978; Wilkinson, 2001; Calagari, 2004; Landtwing et al., 2010). According to this study, there is a close similarity between the microthermometry data of the Kighal deposit and those in the Sungun deposit (Calagari, 1997, 2003, 2004), which has been located in 6 km north of this region.

Microthermometry results of LV and LVS FIs from those samples that were selected from quartz-sulfide and quartz-pyrite veinlets in potassic and phyllic alteration zones and also silica cap-rocks, show that homogenization temperatures and salinity in quartz-sulfide veinlets from potassic alteration zone together with the multiphase FIs have a homogenization temperature of halite T_m (NaCl) from 265 to 450 °C and salinity values from 36 to 59 wt.% NaCl-equiv. These data, as expected, are higher than the phyllic alteration and silica cap-rock two-phase FIs with abundant quantities of homogenization T_h (LV) between 163 and 466 °C and salinity less than 0.3 to 11 wt.% NaCl-equiv. (Fig. 9). The petrographic studies do not show the distribution after trapping such as necking down and stretching in halite-bearing FIs, therefore, association of saline fluid with liquid- and vapor-rich FIs may indicate that some of these inclusions occurred in an immiscible system or boiling condition (Bodnar, 1995; Hedenquist and Richards, 1998).

Based on the homogenization temperature vs. salinity plot for the two-phase LV and multiphase LVS FIs, involved fluids in the Kighal deposit can be divided into four groups: (i) moderate temperature and high salinity, (ii) high temperature and moderate to high salinity, (iii) moderate to high temperature and moderate salinity, (iv) low to moderate temperature and low salinity (Fig. 9). The plot of the multiphase FIs data below the halite saturation curve shows the fluids trapped under unsaturated condition. In Fig. 10, multiphase saline FIs represent a linear decline trend for salinity and temperature which is in accordance with many reported porphyry copper deposits (Cloke and Kesler, 1979; Roedder 1984), emphasizing the presence of high salinity and high temperature fluids derived from magmatic origin. It seems boiling and the development of late hydraulic microfractures affected on the influx and mixing of the primary magmatic fluids with circulating groundwater and eventually leads to formation of the fluids with low temperature and low salinity (Dubessy et al., 2003; Canet et al., 2011).

The diagram of Pirajno (2009) was used to find the effective ligands in transporting of metals in the deposit. Based on Fig. 13, the average measurements of the FIs plots in the chloride complexes field and relatively within sulfide field, therefore, it can be concluded that Cl^- , SO_4^{2-} and/or HS^- complexes transported copper and other elements in the system. The presence of trace amounts of pyrite and chalcopyrite in the Kighal deposit confirm these results.

Based on the homogenization temperature vs. salinity diagram (Wilkinson, 2001), the data for the early stage are located in the field of porphyry deposit and the data for the middle and late stages are located in the field of epithermal deposits (Fig. 14). There is a negative correlation between the homogenization temperature and density values and positive correlation between density and salinity of hydrothermal fluids (Wilkinson, 2001). Hence, the average density in the halite-bearing FIs with high salinity from the potassic alteration samples is more than 1.0 g/cm³ and for the phyllic alteration samples, the density of the two-phase FIs with low salinity is between 0.74 and 0.9 g/cm³. Therefore, with increasing salinity, density of the fluid increases. This wide range of density values indicates that the FIs trapped during boiling and immiscibility occurred between vapor-liquid phases (Wilkinson, 2001). Because of boiling and immiscibility occurrence in the system, there is no need for the fluid pressure correction for homogenization temperatures (Roedder and Bodnar, 1980; Wilkinson, 2001; Chen and Wang, 2011).

There are several methods for estimating of the mineralization depth and pressure of the trapped FIs (Roedder, 1984). Fluid pressure can be estimated by nonboiling FIs and/or boiling bearing inclusions. Nonboiling FIs represent the minimum pressure (Rusk et al., 2008), while boiling bearing inclusions represent more accurate estimations of the trapping pressure based on the microthermometry measurements which have been homogenized by the disappearance of the vapor bubble (Roedder and Bodnar, 1980). Thus, by measuring the trapping pressure, fluids depths can be estimated. Of note, this is not totally correct because the pressure of the fluid system is variable from hydrostatic to lithostatic (Rusk et al., 2008).

According to microthermometry results and the temperature–pressure–depth diagram (Fig. 15) (Sourirajan and Kennedy, 1962; Haas, 1976), the trapping pressures for the early stage (average T_h of 335 °C and salinity of 38 wt.% NaCl-equiv.), were estimated to be within the range of 250–200 bars (average of ~225 bars), which is equivalent to a depth of ~2 km (hydrostatic pressure conditions). The FIs in the middle stage (average

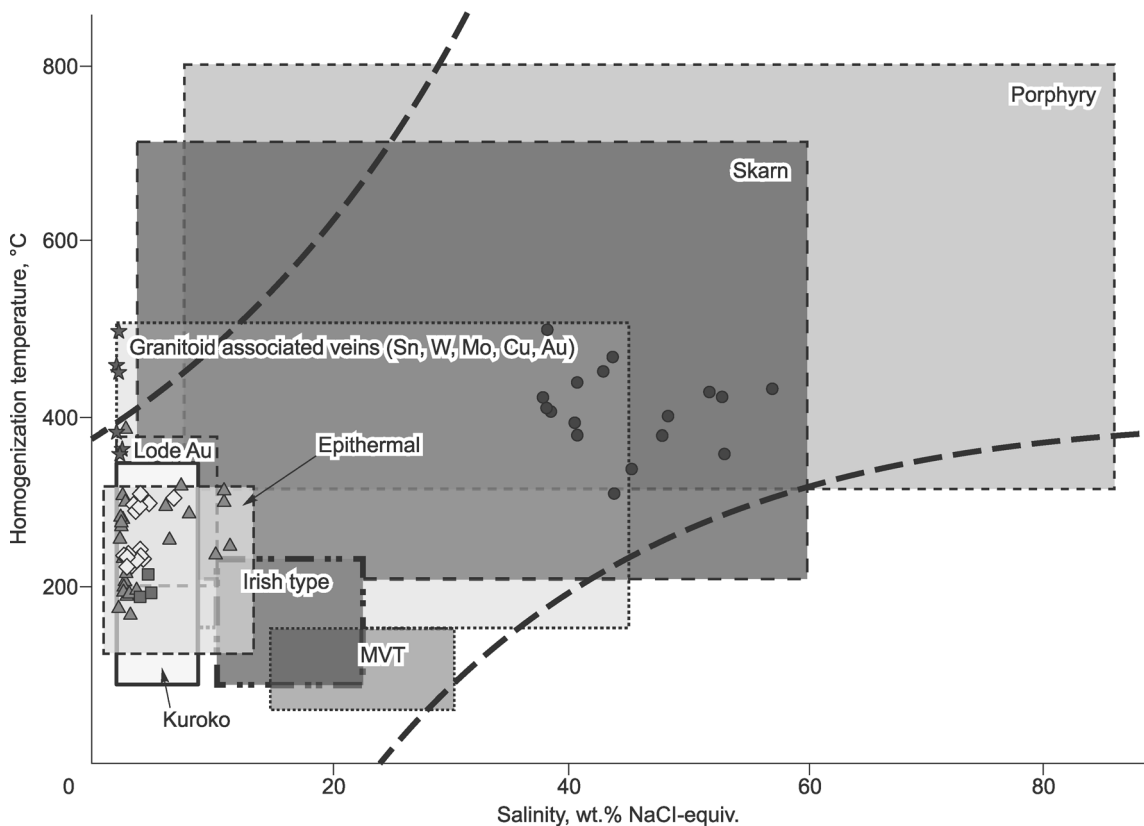


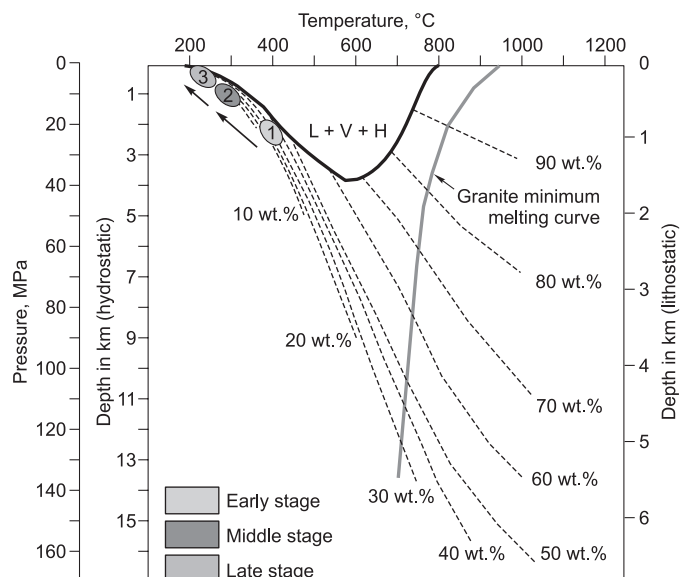
Fig. 14. The diagram for determining mineralization type based on the salinity and temperature of homogenization (Wilkinson, 2001). The Kighal deposit data plot in the porphyry field.

Th of 266 °C and salinity of 2.6 wt.% NaCl-equiv.) yield a trapping depth of ~1500 m (~150 bars hydrostatic pressure conditions). Finally, late stage fluids (average Th of 250 °C and salinity of 2.3 wt.% NaCl-equiv.) yield a depth of <1000 m (<100 bars, hydrostatic pressure conditions). By assuming that the system was closed (lithostatic), the estimated trapping depths are 1 km, 0.5 km, and <0.4 km from early through middle to late stages, respectively. With assumption of an open system for the hydrothermal fluids (hydrostatic), the estimated depths are 2 km, 1.2 km and <1.0 km, for these stages, respectively (Fig. 15).

Simmonds et al. (2015) showed that the two-phase FIs with lower salinity and lower Th have the maximum estimated pressure ranges between 1000 and 2500 bars, while multiphase FIs with higher salinity and higher Th have the minimum estimated pressure ranges between 1000 and 2500 bars. Based on the location of the potassic zone in the center of the system, it is clear that the lithostatic pressure of the potassic zone is much more than that of the phyllic zone. Thus, the wide range of pressure difference between the two-phase and multiphase FIs could be explained by high rates of uplift and erosion of the main part of the deposit and surficial

Fig. 15. Pressure–temperature diagram showing phase relationships in the NaCl–H₂O system at lithostatic and hydrostatic pressures (Fournier, 1999).

L, liquid; V, vapor; H, halite. Thin dashed lines are contours of constant wt.% NaCl dissolved in brine. Location of fluid inclusions assemblages for different stages plotted on it.



cial exposure of potassic alteration in some parts and trapping of low temperature hydrothermal fluids at shallow depths with two-phase low salinity FIs.

The presence of quartz veinlets and crosscutting micro-veinlets shows multiple hydraulic fractures events in the history of the porphyry stock. In general, the estimated depth of mineralization despite of above mentioned incorrect pressure is approximately >1 to 2 km which is similar to the mineralization depth of the porphyry deposits of about 1 to 5 km in worldwide deposits (Pirajno, 2009). Moreover, the similarity between the mineralization depth of the Kighal deposit and mineralization at a depth of 1.5 to 2 km in the Sungun deposit is remarkable (Hezarkhani and Williams-Jones, 1998).

Fluid origin and evolution based on oxygen and hydrogen isotopes

The δD values of the biotite samples from primary magmatic source are between -60 and -100% (Kyser et al., 1982). Biotite samples from potassic alteration in the Kighal deposit are similar to those biotites which were derived from the magmatic source and show δD values between -89 and -82% and $\delta^{18}O$ values in the range of 2.3 to 3.7% . The slightly depleted δD values of the biotite samples in the Kighal deposit reveal the configuration of this hydroxyl mineral from magmatic vapor that experienced large amounts of degassing (Taylor, 1986). Based on isotopic constraints, the fluid which is depleted from remaining δD in the crystallized magma (Taylor, 1986) has an important role in the formation of hydroxyl-bearing minerals and/or degassing occurred in the final stage (Taylor et al., 1983; Harris et al., 2015), so that the degassing magma can explain changes and depletion of the δD in potassic alteration of porphyry copper deposits (Harris et al., 2015).

The fluids with depleted δD values along with potassic alteration associated with the magma degassing process have a great effect on the δD depletion in the residual fluid (Hedenquist and Richards, 1998). Thereby, reducing the δD values of biotite in the potassic alteration zone of the Kighal deposit indicates that the late stage magma lost a lot of its volatiles coinciding with biotite crystallization with depleted δD values (Harris et al., 2005). Thus, the magma degassing mechanism could possibly explain the depleted δD values and isotopic composition of the fluid in the potassic alteration zone of the Kighal deposit. Depletion of δD fluids in the potassic alteration zone of porphyry copper deposits has been previously reported for the Yukon deposit in Canada, and that has been interpreted to be mixing of ancient meteoric waters with saline and high temperature fluids (Sheppard and Taylor, 1974; Selby and Creaser, 2001; Harris et al., 2005). Meanwhile, injection of saline and high temperature magmatic water into the hydrothermal system may explain this depletion trend (Shmulovich et al., 1999). Using the equation of Suzuoki and Epstein's (1976), δD isotope differentiation between biotite and participant waters responsible for biotite formation in the Kighal deposit (ranging from -82 to -89%) (Table 3, Fig. 16) are consistent with magmatic waters (Taylor, 1974).

According to Allegre (2008), $\delta^{18}O$ values of minerals and rocks with a deep magmatic origin are between $+5.0$ and $+8.0\%$. The $\delta^{18}O$ values of the relatively unaltered biotite samples from quartz-monzonite stock range from 2.3 to 3.7% and the calculated $\delta^{18}O$ values of the fluid in equilibrium with biotite are in the range of 4.0 to 5.4% (Zheng, 1993) (Table 3). Therefore, $\delta^{18}O$ values of biotite from the Kighal porphyry stock are similar to the δD values and indicate a magmatic source. The $\delta^{18}O$ values of quartz samples from unmineralized quartz-pyrite veinlets in phyllic and silicic alterations of the Kighal deposit are between 8.0 and 12% and the calculated $\delta^{18}O$ values of the fluid in equilibrium with quartz are in the range of 0.3 to 5.0% (Table 3) (Zhang et al., 1989), which indicates a mixing of magmatic fluids with meteoric waters. Due to the reduction of $\delta^{18}O$ isotopic composition of the fluid from biotite toward quartz as it was expected, the hydrothermal biotite from potassic alteration formed at higher temperatures than the hydrothermal quartz. Overall, all calculated $\delta^{18}O$ data may indicate a dominant magmatic water origin for unmineralized quartz veinlets in the phyllic alteration zone.

Sericite samples from the unmineralized quartz-pyrite veinlets in the phyllic alteration zone show δD values between -85 and -67% and $\delta^{18}O$ values between 6.4 and 10.5% (Table 3), so that the δD values are slightly higher than the primary biotites, but the $\delta^{18}O$ values are slightly lower than the primary biotites and slightly higher than the $\delta^{18}O$ values of quartz. These data indicate that effects of meteoric waters on the development of this alteration system could be insignificant due to fluid-rock interaction (Harris et al., 2005). The $\delta^{18}O$ depletion trend in sericite of the Kighal deposit is similar to other porphyry copper deposits including Santa Rita, Ely and Climax (Sheppard et al., 1971), which these researchers considered this depleting as a result of meteoric waters effect during sericitization. The calculated isotopic composition of the fluid based on the microthermometry results show δD_{H_2O} values of -29.2 to -11.2% (Suzuoki and Epstein, 1976) and $\delta^{18}O_{H_2O}$ values of 4.3 to 8.4% (Zheng, 1993) in equilibrium with sericite, indicating that the isotopic composition of the primary biotites is lighter than sericites and underlines the effect of meteoric waters on magmatic waters (Fig. 16).

Taylor (1997) suggested that meteoric waters play the main role in the formation of phyllic alteration zones in porphyry copper deposits, although many studies showed continuity between high temperature magmatic fluids and hydrothermal and meteoric waters systems in this process (Hedenquist and Richards, 1998;

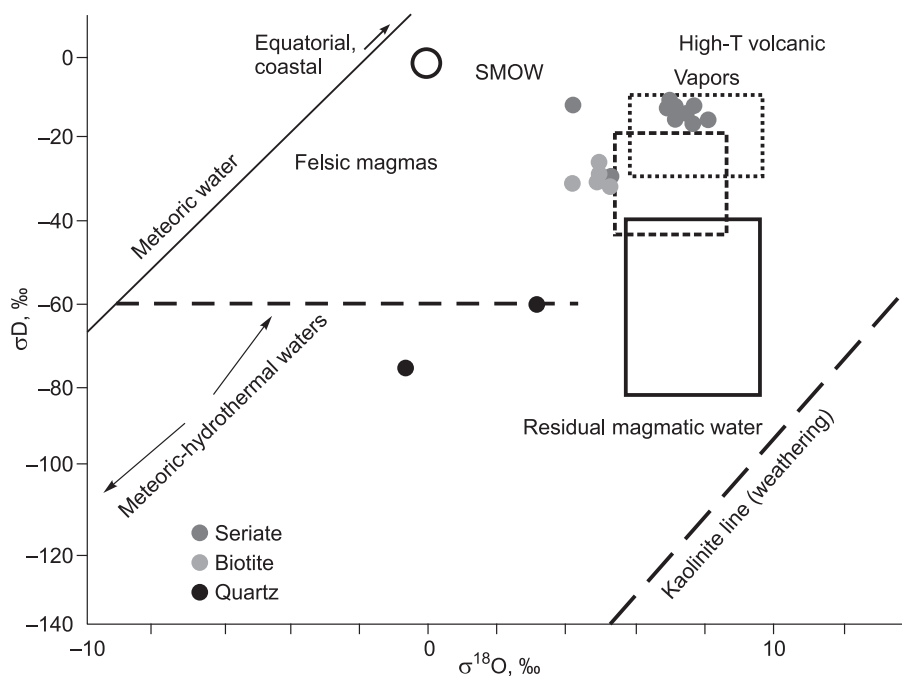


Fig. 16. Plot of δD vs. $\delta^{18}O$ data for biotite, sericite and quartz modified after Sheppard et al. (1971), meteoric water line after Craig (1961) and kaolinite line after Savin and Epstein (1970).

Richards et al., 1998). In the Kighal deposit, similar to other porphyry copper deposits, the deposition of copper minerals occurred in a wide range of temperature from early potassic alteration with temperatures over 400 °C to phyllic alteration with a temperature of 200 to 300 °C.

In this study, it was elucidated that in the Kighal deposit the high temperature saline fluids are responsible for mineralization in the potassic and the overlying/overprinted phyllic alterations. The presence of these sulfides in the phyllic zone in many porphyry copper deposits, indicate that magma is the main source of metals rather than the country wall rocks. Therefore, it can be concluded that mineralization in the phyllic alteration zone in porphyry deposits could be individually achieved by cooling of saline magmatic fluids. As a result, temperature and pH conditions for feldspar destruction are not required for magmatic and meteoric water mixing. Nevertheless, the stable isotopic data indicate that mixing and dilution of magmatic fluids systems by meteoric fluids only occurred at the final stages of the hydrothermal system after cooling to 200 °C and after the main stage of copper mineralization (Harris et al., 2015).

CONCLUSIONS

(1) The Kighal porphyry Cu deposit mainly consists of quartz-monzonite, granodiorite and quartz-diorite porphyries that associated with potassic, phyllic, argillic and propylitic alteration zones. Potassic alteration has had the greatest influence on the quartz-monzonite porphyry, while granodiorite and quartz-diorite intrusions were less affected by this alteration.

(2) Copper mineralization in the Kighal deposit generally occurred in the form of quartz stockworks and veinlets and rarely as disseminated which was frequently observed in the potassic and phyllic alteration zones of quartz-monzonite and granodiorite porphyry stocks.

(3) LVS FIs with high temperature (average of T_{mNaCl} 360 °C) and high salinity (average of 44 wt.% NaCl-equiv.) within the potassic alteration zone indicates that this alteration and associated copper mineralization has been formed by high temperature and high salinity fluids with dominant magmatic origin.

(4) The calculated $\delta^{18}O_{H_2O}$ and δD_{H_2O} values in biotite, sericite and quartz from the potassic and phyllic alteration zones indicates that magmatic fluids were largely responsible for the hydrothermal alterations and subsequent mineralization. Magmatic fluids mixing with meteoric waters in the phyllic alteration zone with temperatures ranges from 300 to 400 °C refers to the low δD values (-68‰) with moderate to high values of $\delta^{18}O$ (6.4 to 10.5‰).

This research is financially supported by the Special Fund of the first author from the Payame Noor University.

REFERENCES

- Aghanabati, A.**, 1991. Magmatic Rocks of Iran, 1: 2,500,000 Survey Sheet. Geological Survey of Iran.
- Aghanabati, A.**, 1998. Major Sedimentary and Structural Units of Iran (Map). *Geosci.* 7, Geological Survey of Iran.
- Allegre, C.J.**, 2008. *Isotope Geology*. Cambridge University Press, New York.
- Alirezaei, S., Ebrahimi, S., Pan, Y.**, 2008. Fluid Inclusion Characteristics of Epithermal Precious Metal Prospects in Northwest Iran. ACROFI-II (Asian Current Research on Fluid Inclusions). Kharagpur, India.
- Berberian, M., King, G.C.**, 1981. Towards a paleogeography and tectonic evolution of Iran. *Can. J. Earth Sci.* 18 (2), 210–265.
- Bodnar, R.J.**, 1995. Hydrothermal fluids and hydrothermal alteration in porphyry copper deposits, in: Wahl, P.W., Bolm, J.G. (Eds.), *Porphyry Copper Deposits of the American Cordillera*. Arizona Geol. Soc., Tucson, pp. 83–93.
- Brenan, J.M., Shaw, H.F., Phinney, D.L., Ryerson, F.J.**, 1994. Rutile-aqueous fluid partitioning of Nb, Ta, Hf, Zr, U and Th: Implications for high field strength element depletions in island-arc basalts. *Earth Planet. Sci. Lett.* 128 (3–4), 327–339.
- Calagari, A.A.**, 1997. Geochemical, Stable Isotope, Noble Gas, and Fluid Inclusion Studies of Mineralization and Alteration at Sungun Porphyry Copper Deposit, East Azarbaijan, Iran: Implication for Genesis. PhD Thesis. Manchester University, Manchester.
- Calagari, A.A.**, 2003. Stable isotope (S, O, H and C) studies of the phyllic and potassic–phyllic alteration zones of the porphyry copper deposit at Sungun, East Azarbaijan, Iran. *J. Asian Earth Sci.* 21 (7), 767–780.
- Calagari, A.A.**, 2004. Fluid inclusion studies in quartz veinlets in the porphyry copper deposit at Sungun, East Azarbaijan, Iran. *J. Asian Earth Sci.* 23 (2), 179–189.
- Canet, C., Franco, S.I., Prol-Ledesma, R.M., González-Partida, E., Villanueva-Estrada, R.E.**, 2011. A model of boiling for fluid inclusion studies: Application to the Bolaños Ag–Au–Pb–Zn epithermal deposit, Western Mexico. *J. Geochem. Explor.* 110 (2), 118–125.
- Chen, Y.J., Wang, Y.**, 2011. Fluid inclusion study of the Tangjiaping Mo deposit, Dabie Shan, Henan Province: implications for the nature of the porphyry systems of post-collisional tectonic settings. *Int. Geol. Rev.* 53 (5–6), 635–655.
- Cloke, P.L., Kesler, S.E.**, 1979. The halite trend in hydrothermal solutions. *Econ. Geol.* 74, 1823–1831.
- Cox, K.G., Bell, J.D., Pakhurst, R.J.**, 1979. *The Interpretation of Igneous Rocks*. Allen and Unwin, London.
- Craig, H.**, 1961. Isotopic variations in meteoric waters. *Science* 133, 1702–1703.
- Davidson, J.P.**, 1996. Deciphering mantle and crustal signatures in subduction zone magmatism, in: Bebout, G.E., Scholl, D.W., Kirby, S.H., Platt, J.P. (Eds.), *Subduction: Top to Bottom*, Geophys. Monogr. Ser., Vol. 96, pp. 251–262.
- De Hoog, J.C.M., Mason, P.R.D., van Bergen, M.J.**, 2001. Sulfur and chalcophile elements in subduction zones: Constraints from a laser ablation ICP-MS study of melt inclusions from Galunggung Volcano, Indonesia. *Geochim. Cosmochim. Acta* 65 (18), 3147–3164.
- Dubessy, J., Derome, D., Sausse, J.**, 2003. Numerical modelling of fluid mixings in the H₂O–NaCl system application to the North Caramal U prospect (Australia). *Chem. Geol.* 194 (1–3), 25–39.
- Etminan, H.**, 1978. Fluid inclusion studies of the porphyry copper ore bodies at Sar-Cheshmeh, Darreh Zar and Mieduk (Kerman region, southeastern Iran) and porphyry copper discoveries at Miduk, Gozan, and Kighal, Azarbaijan region (northwestern Iran), in: Proc. 5th Quadrennial IAGOD Symp. (Snowbird, Utah, 17 August, 1978), p. 88.
- Foley, S.F., Barth, M.G., Jenner, G.A.**, 2000. Rutile/melt partition coefficients for trace elements and an assessment of the influence of rutile on the trace element characteristics of subduction zone magmas. *Geochim. Cosmochim. Acta* 64 (5), 933–938.
- Fournier, R.O.**, 1999. Hydrothermal processes related to movement of fluid from plastic into brittle rock in the magmatic–epithermal environment. *Econ. Geol.* 94 (8), 1193–1211.
- Giggenbach, W.F.**, 1992. Isotopic shifts in waters from geothermal and volcanic systems along convergent plate boundaries and their origin. *Earth Planet. Sci. Lett.* 113 (4), 495–510.
- Haas, J.L. Jr.**, 1976. Physical properties of the coexisting phases and thermochemical properties of the H₂O component in boiling NaCl solutions, in: Haas, J.L. Jr. (Ed.), *Preliminary Steam Tables for NaCl Solutions*. Geol. Surv. Bull. 1421-A.
- Harris, A.C., Golding, S.D., White, N.C.**, 2015. Bajo de la Alumbrera copper-gold deposit: Stable isotope evidence for a porphyry-related hydrothermal system dominated by magmatic aqueous fluids. *Econ. Geol.* 100 (5), 863–886.

Harris, P.T., Heap, A.D., Passlow, V., Sbaffi, L., Fellows, M., Porter-Smith, R., Buchanan, C., Daniell, J., 2005. Geomorphic Features of the Continental Margin of Australia: Report to the National Oceans Office on the Production of a Consistent, High-Quality Bathymetric Data Grid and Definition and Description of Geomorphic Units for Part of Australia's Marine Jurisdiction. Geoscience Australia, Canberra.

Hassanpour, S., 2010. Metallogeny and Mineralization of Cu–Au in Arasbaran Zone (NW Iran). PhD Thesis [in Persian]. University of Shahid Beheshti, Tehran.

Hassanpour, H., Alirezaei, S., Selby, D., Sergeev, S., 2015. SHRIMP zircon U–Pb and biotite and hornblende Ar–Ar geochronology of Sungun, Haftcheshmeh, Kighal, and Niaz porphyry Cu–Mo systems: evidence for an early Miocene porphyry-style mineralization in northwest Iran. *Int. J. Earth Sci.* 104 (1), 45–59.

Hedenquist, J.W., Richards, J.P., 1998. The influence of geochemical techniques on the development of genetic models for porphyry copper deposits, in: Richards, J.P., Larson, P.B., (Eds.), *Techniques in Hydrothermal Ore Deposits Geology*. *Rev. Econ. Geol.*, Vol. 10, pp. 235–256.

Heinrich, C.A., Pettke, T., Halter, W.E., Aigner-Torres, M., Audetat, A., Gunther, D., Hattendorf, B., Bleiner, D., Guillong, M., Horn, I., 2003. Quantitative multi-element analysis of minerals, fluid and melt inclusions by laser-ablation inductively-coupled-plasma mass-spectrometry. *Geochim. Cosmochim. Acta* 67 (18), 3473–3497.

Hezarkhani, A., Williams Jones, A.E., Gammons, C., 1997. Copper solubility and deposition conditions in the potassic and phyllic alteration zones, at the Sungun Porphyry Copper Deposit, Iran, in: *Proc. GAC–MAC, Annual Meeting, Canada, Ottawa, Vol. 50, A-67.*

Hezarkhani, A., Williams-Jones, A.E., 1998. Controls of alteration and mineralization in the Sungun porphyry copper deposit, Iran: Evidence from fluid inclusions and stable isotopes. *Econ. Geol.* 93 (5), 651–670.

Irvine, T.N., Baragar, W.R.A., 1971. A guide to the chemical classification of common volcanic rocks. *Can. J. Earth Sci.* 8 (5), 523–548.

Kay, S.M., Ambruzzi, J.M., 1996. Magmatic evidence for Neogene lithospheric evolution of the central Andean “flat-slab” between 30° S and 32° S. *Tectonophysics* 259 (1-3), 15–28.

Kyser, T.-K., O’Neil, J.R., Carmichael, I.S.E., 1982. Genetic relations among basic lavas and ultramafic nodules: evidence from oxygen isotope compositions. *Contrib. Mineral. Petrol.* 81 (2), 88–102.

Landtwing, M.R., Furrer, C., Redmond, P.B., Pettke, T., Guillong M., Heinrich, C.A., 2010. The Bingham Canyon porphyry Cu–Mo–Au deposit: III. Zoned copper-gold ore deposition by magmatic vapor expansion. *Econ. Geol.* 105 (10), 91–118.

Mavrogenes, J.A., Bodnar, R.J., 1994. Hydrogen movement into and out of fluid inclusions in quartz: Experimental evidence and geologic implications. *Geochim. Cosmochim. Acta* 58 (1), 141–148.

Mehrpour, M., 1993. Contributions to the Geology, Geochemistry, Ore Genesis and Fluid Inclusion Investigations on Sungun Cu–Mo Porphyry Deposit, Northwest of Iran. PhD Dissertation. Univ. Hamburg, Hamburg.

Miyashiro, A., 1974. Volcanic rock series in island arcs and active continental margins. *Am. J. Sci.* 274 (4), 321–355.

Nash, J.T., 1976. Fluid Inclusion Petrology—Data from porphyry copper Deposits and Applications to Exploration. US Geol. Surv., Prof. Pap. 907–D, US Government Printing Office, Washington.

Niazi, M., Asudeh, I., Ballard, G., Jackson, J., King, G., McKenzie, D., 1978. The depth of seismicity in the Kermanshah region of the Zagros Mountains, Iran. *Earth Planet. Sci. Lett.* 40 (2), 270–274.

NICICO, 2006. Geology and Alteration Studies on Kighal Area, Zarnab Ekteshaf [in Persian].

Omrani, J., Agard, P., Whitechurch, H., Benoit, M., Prouteau, G., Jolivet, L., 2008. Arc-magmatism and subduction history beneath the Zagros Mountain, Iran: A new report of adakites and geodynamic consequences. *Lithos* 106 (3), 380–398.

Pearce, J.A., Harris, N.B.W., Tindle, A.G., 1984. Trace element discrimination diagrams for the tectonic interpretation of granitic rocks. *J. Petrol.* 25 (4), 956–983.

Peccerillo, R., Taylor, S.R., 1976. Geochemistry of Eocene calc-alkaline volcanic rocks from the Kastamonu area, northern Turkey. *Contrib. Mineral. Petrol.* 58 (1), 63–81.

Pirajno, F., 2009. *Hydrothermal Processes and Mineral Systems*. Springer / Geol. Surv. Western Australia, Dordrecht, London.

Pourhosseini, F., 1981. Petrogenesis of Iranian Plutons, a Study of the Natanz and Bazman Intrusive Complexes. PhD Thesis. Univ. Cambridge, Cambridge.

Richards, J.P., 2011. Magmatic to hydrothermal metal fluxes in convergent and collided margins. *Ore Geol. Rev.* 40 (1), 1–26.

- Richards, J.P., Krogh, T.E., Spooner, E.T.C.**, 1998. Fluid inclusion characteristics and U–Pb rutile age of late hydrothermal alteration and veining at the Musoshi stratiform copper deposit, Central African copper belt, Zaire. *Econ. Geol.* 83 (1), 118–139.
- Roedder, E.**, 1984. Fluid inclusions, in: Ribbe, P.E. (Ed.), *Reviews in Mineralogy*. Vol. 12. Mineral. Soc. Am. Book Crafters, Michigan.
- Roedder, E., Bodnar, R.J.**, 1980. Geologic pressure determination from fluid inclusion studies. *Annu. Rev. Earth Planet. Sci.* 8, 263–301.
- Rusk, B.G., Reed, M.H., Dilles, J.H.**, 2008. Fluid inclusion evidence for magmatic-hydrothermal fluid evolution in the porphyry copper-molybdenum deposit at Butte, Montana. *Econ. Geol.* 103 (2), 307–334.
- Savin, S.M., Epstein, S.**, 1970. The oxygen and hydrogen isotope geochemistry of clay minerals. *Geochim. Cosmochim. Acta* 34 (1), 25–42.
- Seedorff, E., Dilles, J.D., Proffett, J.M. Jr., Einaudi, M.T., Zurcher, L., Stavast, W.J.A., Johnson, D.A., Barton, M.D.**, 2005. Porphyry deposits: characteristics and origin of hypogene features, in: Hedenquist, J.W., Thompson, J.F.H., Goldfarb, R.J., Richards, J.P. (Eds.), *Econ. Geol. 100th Anniversary Volume*. Society of Economic Geologists, Littleton, CO, USA, pp. 251–298.
- Selby, D., Creaser, R.A.**, 2001. Re–Os geochronology and systematics in molybdenite from the Endako porphyry molybdenum deposit, British Columbia, Canada. *Econ. Geol.* 96 (1), 197–204.
- Shafiei, B., Haschke, M., Shahabpour, J.**, 2009. Recycling of orogenic arc crust triggers porphyry Cu mineralization in Kerman Cenozoic arc rocks, southeastern Iran. *Miner. Deposita* 44, 265–283.
- Sheppard, S.M.F., Nielsen, R.L., Taylor, H.P. Jr.**, 1971. Hydrogen and oxygen isotope ratios in minerals from porphyry copper deposits. *Econ. Geol.* 66 (4), 515–542.
- Sheppard, S.M.F., Taylor, H.P. Jr.**, 1974. Hydrogen and oxygen isotope evidence for the origin of water in the Boulder batholith and the Butte ore deposit, Montana. *Econ. Geol.* 69 (6), 926–946.
- Shepherd, T., Rankin, A.H., Alderton, D.H.M.**, 1985. *A Practical Guide to Fluid Inclusion Studies*. Blackie, London.
- Shimizu, H., Sawatari, H., Kawata, Y., Dunkley, P.N., Masuda, A.**, 1992. Ce and Nd isotope geochemistry on island arc volcanic rocks with negative Ce anomaly: existence of sources with concave REE patterns in the mantle beneath the Solomon and Bonin island arcs. *Contrib. Mineral. Petrol.* 110 (2/3), 242–252.
- Shmulovich, K.I., Landwehr, D., Simon, K., Heinrich, W.**, 1999. Stable isotope fractionation between liquid and vapor in water–salt systems up to 600 °C. *Chem. Geol.* 157 (3–4), 343–354.
- Sillitoe, R.H.**, 1997. Characteristics and controls of the largest porphyry copper-gold and epithermal gold deposits in the Circum–Pacific region. *Aust. J. Earth Sci.* 44 (3), 373–388.
- Sillitoe, R.H.**, 2000. Gold-rich porphyry deposits: Descriptive and genetic models and their role in exploration and discovery, in: Hagemann, S.G., Brown, P.E. (Eds.), *Gold in 2000*. *Rev. Econ. Geol.* 13, 315–345.
- Simmonds, V.**, 2013. Geochemistry and petrogenesis of an adakitic quartz-monzonitic porphyry stock and related cross-cutting dike suites, Kighal, northwest Iran. *Int. Geol. Rev.* 55 (9), 1126–1144.
- Simmonds, V., Calagari, A.A., Moayyed, M., Jahangiri, A.**, 2012. Study of porphyry-type alteration zones and geochemical behavior of trace and rare earth elements within them in Kighal, north of Varzeghan, East-Azarbaidjan, Iran. *Iran J. Crystallogr. Miner.* 19 (4), 565–578.
- Simmonds, V., Calagari, A.A., Kyser, K.**, 2015. Fluid inclusion and stable isotope studies of the Kighal porphyry Cu–Mo prospect, East-Azarbaidjan, NW Iran. *Arab. J. Geosci.* 8 (1), 437–453.
- Sohrabi, G.H.**, 2015. Study of Metallogeny and Geochemistry of Molybdenum Deposits in Gharadagh–Sivardagh Belt, East Azarbaidjan, NW Iran. Unpublished PhD Thesis [in Persian]. Univ. Tabriz, Tabriz.
- Sourirajan, S., Kennedy, G.C.**, 1962. The system H₂O–NaCl at elevated temperatures and pressures. *Am. J. Sci.* 260 (2), 115–141.
- Stampfli, G.M.**, 2000. Tethyan Ocean, in: Bozkurt, E., Winchester, J.A., Piper, J.D.A. (Eds.), *Tectonics and Magmatism in Turkey and Surrounding Area*. *Geol. Soc. London, Spec. Publ.* 173, 1–23.
- Sun, S.S., McDonough, W.F.**, 1989. Chemical and isotopic systematics of oceanic basalts: Implications for mantle composition and processes, in: Saunders, A.D., Norry, M.J. (Eds.), *Magmatism in the Ocean Basins*. *Geol. Soc. London. Spec. Publ.* 42, 315–345.
- Suzuoki, T., Epstein, S.**, 1976. Hydrogen isotope fractionation between OH-bearing minerals and water. *Geochim. Cosmochim. Acta* 40 (10), 1229–1240.
- Tatsumi, Y., Hamilton, D.L., Nesbitt, R.W.**, 1986. Chemical characteristics of fluid phase released from a subducted lithosphere and origin of arc magmas: Evidence from high-pressure experiments and natural rocks. *J. Volcanol. Geotherm. Res.* 29, 293–309.
- Taylor, B.E.**, 1986. Magmatic volatiles: Isotopic variation of C, H, and S. *Rev. Mineral. Geochem.* 16 (1), 185–225.

Taylor, B.E., Eichelberger, J.C., Westrich, H.R., 1983. Hydrogen isotopic evidence of rhyolitic magma degassing during shallow intrusion and eruption. *Nature* 306, 541–545.

Taylor, H.P., 1974. The application of oxygen and hydrogen isotope studies to problems of hydrothermal alteration and ore deposition. *Econ. Geol.* 69 (6), 843–883.

Taylor, H.P., 1997. Oxygen and hydrogen isotope relationships in hydrothermal mineral deposits, in: Barnes, H.L. (Ed.), *Geochemistry of Hydrothermal Ore Deposits* (3rd ed.). J. Wiley and Sons, New York, pp. 229–302.

Wyman, D.A., 1999. A 2.7 Ga depleted tholeiite suite: evidence of plume-arc interaction in the Abitibi Greenstone Belt, Canada. *Precambrian Res.* 97 (1–2), 27–42.

Wilkinson, J.J., 2001. Fluid inclusions in hydrothermal ore deposits. *Lithos* 55 (1–4), 229–272.

Zhang, Y.G., Frantz, J.D., 1987. Determination of the homogenization temperatures and densities of supercritical fluids in the system NaCl–KCl–CaCl₂–H₂O using synthetic fluid inclusions. *Chem. Geol.* 64 (3–4), 335–350.

Zhang, L.-G., Liu J.-X., Zhou H.B., Chen Z.-S., 1989. Oxygen isotope fractionation in the quartz–water–salt system. *Econ. Geol.* 84 (6), 1643–1650.

Zheng, Y.-F., 1993. Calculation of oxygen isotope fractionation in hydroxyl-bearing silicates. *Earth Planet. Sci. Lett.* 120 (3–4), 247–263.

*Рекомендована к печати 22 мая 2019 г.
Н.В. Соболевым*

*Поступила в редакцию 30 июля 2018 г.,
после доработки — 5 апреля 2019 г.*